Aerosol Optical Properties Derived from the DRAGON-NE Asia campaign, and Implications for Single Channel Algorithm to Retrieve Aerosol Optical Depth in spring from Meteorological Imager (MI) On-board Communication, Ocean and Meteorological Satellite (COMS)

Mijin Kim[1], Jhoon Kim[1,*], Ukkyo Jeong[1], Woogyung Kim[1], Hyunkee Hong[2], Brent Holben[3], Thomas F. Eck[3,4], Jae Hyun Lim[5], Chang Keun Song[5], Sukjo Lee[5,+] and Chu-Yong Chung[6]

[1] Department of Atmosphere Sciences/IEAA BK 21 plus, Yonsei University, Seoul, Korea

[2] Department of Spatial Information Engineering, Pukyong National University, Busan, Korea

[3] NASA Goddard Space Flight Center, Greenbelt, MD, USA

[4] Universites Space Research Association, Columbia, MD, USA

[5] National Institute of Environmental Research (NIER), Inchon, Korea

[+] Now at Asia Center for Air Pollution Research (ACAP), Niigata-shi, Japan

[6] National Meteorological Satellite Center, Jincheon-gun, Chungcheongbuk-do, Korea

*Corresponding author.

Institute of Earth, Astronomy, and Atmosphere, Brain Korea 21 Plus Program, Department of Atmospheric Sciences, Yonsei University, Seoul, Republic of Korea

Tel.: +82-2-2123-5682, Fax: +82-2-365-5163

E-mail address: jkim2@yonsei.ac.kr (Jhoon Kim)

Abstract

Aerosol model optimized for North East Asia is updated with the inversion data from the Distributed Regional Aerosol Gridded Observation Networks (DRAGON)-Northeast (NE) Asia campaign during spring from March to May in 2012. This updated aerosol model was then applied to a single visible channel algorithm to retrieve aerosol optical depth (AOD) from a Meteorological Imager (MI) on-board the geostationary meteorological satellite, Communication Ocean and Meteorological Satellite (COMS). This model plays an important role in retrieving accurate aerosol optical depth (AOD) from a single visible channel measurement. For the single channel retrieval, sensitivity tests showed that perturbations by 4 % (0.926±0.04) in the assumed single scattering albedo (SSA) can result in the retrieval error in AOD by over 20%. Since the measured reflectance at top-of-atmosphere depends on both AOD and SSA, the overestimation of assumed SSA in aerosol model leads to an underestimation of AOD. Based on the AErosol RObotic NETwork (AERONET) inversion datasets obtained over East Asia before 2011, seasonally analyzed AOPs was categorized by SSAs at 675 nm of 0.92±0.035 for spring (March, April, and May). After the DRAGON-NE Asia 2012, the SSA during spring showed a slight increase to 0.93±0.035. In terms of the volume size distribution, the mode radius of coarse particles were increased from 2.08±0.40 to 2.14±0.40. While the original aerosol model consists of volume size distribution and refractive indices obtained before 2011, the new model is constructed by using total dataset after the DRAGON-NE Asia campaign. The large volume of dataset in high spatial resolution from this intensive campaign can be used to improve the representative aerosol model for East Asia.

Accordingly, the ’new’ AOD datasets retrieved from a single channel algorithm, which uses a pre-calculated look-up table (LUT) with the new aerosol model, show an improved correlation with the measured AOD during the DRAGON-NE Asia campaign. The correlation between the new AOD and AERONET value shows regression slope of 1.00, while the comparison of the ‘original AOD’ retrieved using the original aerosol model shows the slope of 1.08. The change of y-offset is not significant, and the correlation coefficients for the comparisons of the original and new AOD are 0.87 and 0.85, respectively. The tendency of the original aerosol model to overestimate the retrieved AOD is significantly improved by using the SSA values in addition to size distribution and refractive index obtained using the new model.

Keywords: Aerosol optical depth, Single channel algorithm, DRAGON-NE Asia 2012

1. Introduction

An understanding of global aerosol distribution and its optical characteristics is important not only for predictions related to climate change, but also for monitoring the effects of changing air quality on human health. It is widely accepted that aerosol has both direct and indirect effects on the Earth radiation budget (IPCC, 2013). Aerosols are also linked to respiratory illness (e.g. Pope and Dockery, 2006) and meningitis epidemics (e.g. Deroubaix et al., 2013). Since the global aerosol distribution shows high spatial and temporal variability, many studies have developed aerosol retrieval algorithms utilizing both low earth orbit (LEO) satellite measurements (Hsu et al., 2004; Kim et al., 2007; Torres et al., 2007; Kahn et al., 2010; Lyapustin et al., 2011b; von Hoyningen-Huene et al, 2011; Wong et al., 2010; Bevan et al., 2012; Sayer et al., 2012; Levy et al., 2013) and geostationary orbit (GEO) satellite measurements (Knapp et al., 2002, 2005; Wang et al., 2003; Urm and Sohn, 2005; Yoon et al., 2007; Kim et al., 2008; Lee et al., 2010b; Zhang et al., 2011; Kim et al., 2014). These studies have typically adopted an inversion approach, using a pre-calculated look-up table (LUT) based on assumed aerosol optical properties (AOPs) to retrieve aerosol information from the measured visible reflectance at the top of the atmosphere. In this method, the accurate estimation of surface reflectance and assumption of optimized aerosol optical type are key to retrieve accurate aerosol information. The surface information was taken account by using single view algorithm based on multi-channel algorithm with certain assumption (e.g. Levy et al., 2007b), or by using multiple view algorithms for the Multi-angle Advanced Along-Track Scanning Radiometer (AATSR) (Grey et al., 2006) or the Polarization and Directionality of Earth Reflectances (POLDER) sensor (Waquet et al., 2009)

90 measurement. Under conditions of low aerosol optical depth (AOD), the estimation of
91 surface reflectance is most crucial to retrieve accurate AOD, while assumptions about
92 the type of aerosol are more significant for cases with higher AOD. A variation in
93 single scattering albedo (SSA) of ±3% (based on a reference value of 0.90) results in a
94 10% error for moderate AOD (τ = 0.5 at 0.67 μm) and a 32% error for large AODs (τ
95 = 1.5) (Zhang et al., 2001). Lee et al. (2012) used a tri-axial ellipsoidal database of
96 dust (Yang et al., 2007) and inversion data from the Aerosol Robotic Network
97 (AERONET) to greatly improve the AOD retrieved using the MODIS dark target
98 algorithm with regards to its Pearson coefficient (from 0.92 to 0.93), regression slope
99 (from 0.85 to 0.99), and the percentage of data within an expected error bound (from
100 62% to 64%).
101 Ground-based measurements are essential to the construction of a well-defined
102 aerosol model to calculate LUT. Aerosol observations from ground-based sun/sky
103 radiometer measurements, such as the AERONET, provide accurate global and local
104 AOPs, including AOD and particle characteristics (Duvobik et al., 2000; Holben et al.,
105 1998). Numerous aerosol models for satellite aerosol algorithms have been based on
106 the AERONET datasets (e.g. Sayer et al., 2014), and these models can be further
107 improved by using AOPs obtained from intensive field campaigns in high spatial
108 resolution (e.g. Huebert et al., 2003; Nakajima et al., 2007). Recently, the Distributed
109 Regional Aerosol Gridded Observation Networks (DRAGON)-Northeast (NE) Asia
110 2012 campaign over South Korea and Japan, during spring from March to May 2012,
111 provided a valuable insight into the characteristics of aerosol over metropolitan areas
112 (http://aeronet.gsfc.nasa.gov/new_web/DRAGONAsia_2012_Japan_South_Korea.ht
113 ml). The campaign studied aerosol characteristics over known polluted areas affected
114 by diverse aerosol sources such as urban pollutants and transported dust. In addition,

115 the high-spatial resolution data from the campaign were used to validate the satellite
116 aerosol algorithms covering the same region.
117 To investigate the role of the mesoscale network of ground-based aerosol
118 measurements in the satellite-based AOD retrieval, an aerosol retrieval algorithm
119 based on the inversion method is tested in this study. By using a single-visible
120 measurement of Meteorological Imager (MI) on-board the Communication, Ocean,
121 and Meteorological Satellite (COMS), an AOD retrieval algorithm was developed by
122 Kim et al. (2014), and provides valuable results regarding aerosol distribution and
123 transport. Since the algorithm cannot detect temporal and spatial variation of AOPs,
124 the single type of assumed, optimized aerosol model was used as previous studies (e.g.
125 Knapp et al., 2002; Yoon, 2006; Yoon et al., 2007; Wang et al., 2003). In this regard,
126 the representative aerosol model is important to reduce the uncertainty in AOD
127 retrieval. Here, the aerosol model is newly analysed from the previous study (Kim et
128 al., 2014) by using extended dataset after the DRAGON-NE Asia campaign. The
129 campaign which focuses on the monitoring of aerosol properties over Korea and
130 Japan can provide details of aerosol distribution, and contribute to accumulate the
131 data set. The new aerosol model applied to the single channel algorithm, and the
132 retrieved AODs are compared with directly measured values from the DRAGON-NE
133 Asia campaign.
134 The single channel algorithm used in this study is similar in nature to that described
135 by Kim et al. (2014), which improved the basic single channel algorithm by applying
136 the critical reflectance method and background AOD (BAOD) correction. To consider
137 the importance of the aerosol type selection, the algorithm applied the critical
138 reflectance method (Fraser and Kaufman, 1985) to determine the SSA for each
139 measured scene over urban areas. Meanwhile, the BAOD, representing the persistent

concentration of aerosol even in the clearest air condition, was estimated by finding the minimum AOD among the long-term measurement. Since the algorithm estimated surface reflectance based on the minimum reflectance method, underestimation or neglect of the BAOD results in the overestimation of the surface reflectance, and thus leads to the underestimation of AOD (Knapp et al., 2002; Yoon, 2006). The correction for BAOD to the surface reflectance showed significant effects in the Kim et al. (2014), and is also considered here, whereas the critical reflectance method is not adopted to evaluate the effects of assumed aerosol property to the AOD retrieval.

Though the accuracy of AOD retrieved from the single channel algorithm is limited because of the limitation in type detection, the products obtained from GEO measurement has an advantage of continuous monitoring of aerosol emission and transport from source region in high temporal resolution. The continuous monitoring is expected to improve the capabilities to predict ambient aerosol properties (e.g. Saide et al., 2014; Park et al., 2014).

The datasets used in this study are summarized in section 2, and details of the single channel algorithm and its results are described in section 3. Modifications to the aerosol model using data from the DRAGON-Asia campaign, and their effects on subsequent retrievals, are outlined in section 4.

2. Data

2.1. DRAGON-NE Asia Campaign

The AERONET, a network of globally distributed ground-based sun photometers, is widely used to understand global AOPs and to validate satellite-based aerosol

products. The AERONET sun photometer measurements of direct solar radiation provide accurate measurements of AOD (~0.01 in the visible and near-infrared and ~0.02 in the UV) under cloud-free conditions (Eck et al., 1999; Holben et al., 1998; Holben et al., 2001), and sky radiance measurements in an almucantar scenario can be inverted to calculate AOPs such as size distribution, single scattering albedo, phase functions, and the complex index of refraction (Dubovik and King, 2000; Dubovik et al., 2000; Dubovik et al., 2002).

During the DRAGON-NE Asia campaign in 2012, 20 Cimel sun-sky radiometer instruments were deployed in Seoul, as well as in eastern and western parts of South Korea. In Japan, about 20 instruments were deployed in Osaka, West Japan and Fukushima valley. The distribution of DRAGON-Korea and -Japan sites is shown in Figure 1, along with the number of AOD data provided in level 2.0 (cloud screened and quality assured; Smirnov et al., 2000) direct products during the campaign. Those deployed sun photometers provided the high spatial-resolution information to address characteristics of mega-city aerosol. Figure 2 shows average and standard deviation for each of AOD (500 nm) and Ångström Exponent (AE, 440 – 870 nm) measured during the campaign. In Figure 2(a), the average AOD ranged between 0.23 and 0.52, and showed a decreasing behavior towards southeast. The maximum value of 0.52 was found at two sites in Fukue (128.68°E, 32.75°N) and Sanggye (127.07°E, 37.66°N), while the minimum value of 0.23 was found at Kohriyama site (140.38°E, 37.36°N). In terms of local average, the mean AOD of 0.43 in Seoul was higher than the value of 0.30 in Osaka. Similarly, the standard deviation of AOD in Figure 2(b) was low in the eastern part of Korea. While the standard deviation varied between 0.22 and 0.31 in Seoul, the values in Japan were between 0.11 and 0.16. The regional difference was figured out also in terms of AE in Figure 2(c). The respective average

AE of 1.20 and 1.27 in Seoul and Osaka represents that the particle size in Seoul is larger than that of Osaka, in general. The spatial distributions of AOD and AE can be related closely with transport of aerosol in East Asia during winter and spring (Park et al., 2014).

In this study, the extensive AERONET inversion data (level 2.0 daily products) over East Asia (20°N–50°N, 95°E–145°E) were used to analyse optimized AOPs; the retrieved volume size distribution and complex refractive indices, which are utilized to compute the spectral SSA. Duvobik et al. (2000) recommended that the quality of refractive index and SSA becomes reliable when the AOD (440 nm) is higher than 0.4 and solar zenith angle is higher than 45 °. To avoid insufficient data points for low AOD case, the daily averaged product were applied. Level 2.0 AOD datasets measured for the DRAGON-NE Asia 2012 campaign with more than 50 data points were used to validate the retrieval results. The AERONET sites used, including the campaign sites, are listed in Table 1, along with the period of the inversion products. The campaign sites are numbered, and sites indicated by bold character represent the validation site selected randomly to test the consistency of the retrieval accuracy. The inversion products obtained at those validation sites were not applied to analyse the aerosol model, but direct AOD products were used to validate the algorithm. While a total of 12,126 inversion datasets from 1999 to 2012 were compiled, 84,091 AOD datasets at 39 sites in spring of 2012 were applied from the campaign.

2.2. COMS Meteorological Imager

A multi-purpose geostationary satellite, COMS, designed to orbit at a longitude of 128.2°E, was launched on June 27, 2010 by the Korean government. The satellite

215 performs meteorological and ocean monitoring by using the MI and Geostationary
216 Ocean Color Imager (GOCI) instruments. The MI measures the single visible
217 reflectance (0.55–0.80 μm) at a 1 km spatial resolution, and the brightness
218 temperature (BT) at four IR wavelengths at a 4 km spatial and 30 min temporal
219 resolution. The four IR channels cover spectral ranges of 10.3–11.3 (IR1), 11.5–12.5
220 (IR2), 6.5– 7.0 (IR3), and 3.5–4.0 μm (IR4). The MI can cover a full disk from its
221 equatorial position at 128.2°E, though this study focuses mainly on images from East
222 Asia. The MI measurement from the single visible and four IR channels are applied to
223 retrieve land and ocean surface temperature, incoming and outgoing radiance, and
224 atmospheric variables including aerosol, cloud properties, precipitable water, and
225 upper tropospheric humidity. The level2 products can be found from the National
226 Meteorological Satellite Center (http://nmsc.kma.go.kr/html/homepage/ko/main.do)
227 of Korea.
228
229 **2.3. MODIS AOD**
230
231 To estimate the BAOD distribution over East Asia over long period, an AOD product
232 at 10×10 km^2 resolutions from the Moderate Resolution Imaging Spectroradiometer
233 (MODIS) was used (Collection 5.1; MYD04_Lv2.0). The AOD at 550 nm from a
234 dark target algorithm (Levy et al., 2007b, 2010; Remer et al., 2005) was interpolated
235 onto a grid of 0.25° × 0.25° to find the minimum value for each area. Considering
236 spatial variation of BAOD, the MODIS product was applied to cover wider area over
237 long term, although satellite measurement has larger uncertainty than the ground-
238 based measurement. The expected error in the AOD product is ±(0.05 + 15%), and

239 over 66% of the retrieved AODs from the MODIS algorithm lie within the error range,
240 with a correlation coefficient of 0.9 (Levy et al., 2010). Despite of the seasonal
241 variation of atmospheric condition over North East Asia, the seasonal variation of the
242 BAOD was not considered because of insufficient data points for winter and summer
243 depending on snow surface and summer monsoon. The uncertainty related with the
244 BAOD assumption will be discussed in section 3.5.
245
246 **3. Single channel algorithm**
247
248 The basic concept of the single channel algorithm suggested in Kim et al. (2014) lies
249 in the inversion of the TOA reflectance to AOD by using the sensitivity of the TOA
250 reflectance to AOD under the condition of fixed aerosol model, with known geometry
251 and retrieved surface reflectance. The sensitivities of the reflectance to each variable
252 are from a forward-model, RTM, assuming certain microphysical properties for the
253 aerosol. The results are compiled into a LUT, where the assumed characteristics of the
254 AOPs form the basis for the aerosol model. Generally, the LUT for a single channel
255 algorithm lists the calculated reflectance as a function of AOD, surface reflectance,
256 measurement geometry, and the assumed aerosol model. In this study, a dynamic
257 aerosol model was constructed using long-term AERONET inversion data to consider
258 changes in refractive index, the mode radius and the width (standard deviation) in the
259 volume size distribution with respect to the AOD. The volume size distribution
260 consists of two modes, fine and coarse, and both vary in accordance with assumed
261 AOD in the RTM simulation. In addition, the aerosol model was designed to include
262 the seasonal variation in AOPs, with a different LUT selected depending on the
263 season in which the measurement was taken. A flowchart of the AOD retrieval

algorithm for MI measurements is shown in Figure 3. To estimate surface reflectance, the minimum reflectance method was applied under the assumption that the increase in AOD makes a positive contribution to TOA reflectance over a dark surface. The minimum TOA reflectance obtained from the previous 30-day measurement was converted to surface reflectance, after correcting for scattering by atmospheric molecules and for BAOD.

3.1. Cloud masking

The AOD was retrieved only for cloud-free pixels satisfying threshold tests of TOA reflectance and brightness temperature (BT). The threshold of 0.35 for the TOA reflectance at the visible channel separated bright cloud pixel, and the threshold of 5 K for the BT difference between the maximum BT for the previous 30 days and the BT of the current pixel separated cold cloud pixel. The pixels which have BT lower than 265 K were also masked out. Additionally, thresholds for BT differences between IR1 and IR2, and IR1 and IR4 were taken from Frey et al. (2008). The thresholds to distinguish cloud and aerosol pixel (IR1-IR2 BTD), and to detect low level cloud (IR1-IR4 BTD) were adjusted as follows by trial and error. The positive BTD between IR1 and IR2, and the largely negative BTD (< -6K) were found in cloud pixel. Thus, the cloud masking procedure includes the following tests:

$$\text{Visible reflectance} > 0.35$$

$$\text{IR1-IR2} > 0.5\ \text{K} \ \&\ \text{IR1} < 268\ \text{K}$$

$$\text{IR1-IR2} > 0.5\ \text{K} \ \&\ \text{IR1max-IR1} > 5\ \text{K}$$

$$\text{IR1-IR2} > 1.5\ \text{K} \ \&\ \text{IR1-IR4} < -6\ \text{K for Ocean}$$

IR1-IR2 > 0.5 K & IR1-IR4 < -10 K for Ocean

IR1-IR2 > 1.5 K & IR1-IR4 < -14 K for Land

3.2. Surface reflectance and BAOD

The BAOD represents a residual AOD value even in the clearest conditions; i.e. the minimum AOD for each location. According to analyses of global AERONET direct measurements, the minimum AOD over urban areas or near an aerosol source region is non-zero due to the steady emission of aerosol (Kim et al., in preparation). An underestimation of BAOD results in an underestimation of retrieved AOD. In an environment of continuous development, population growth, and desertification, the BAOD is not negligible, particularly over East Asia. Accordingly, Kim et al. (2014) used the monthly BAOD obtained from AERONET direct measurements in Hong Kong for AOD retrieval in the region. Subsequently, the BAOD was estimated from the MODIS AOD product for 7 years from 2006 to 2012, and used here in order to take advantage of the fine spatial resolution of the satellite measurements. The BAOD ranged from 0.00 to 0.56, with an average value of 0.03 (Figure 4). Over ocean, spatial variation of BAOD was not significant because the background aerosol is most likely sea-salt with the median value of 0.022. Over land, however, the spatial distribution of BAOD was related to surface type. While the median of BAOD over land was 0.017, the values near metropolitan areas such as Beijing, Seoul, Tokyo, and Hong Kong were generally higher than 0.1. Over the industrialized region located in the lower reaches of the Yangtze River and near Hong Kong, the values even reached over 0.30. Conversely, the region located far from the aerosol source showed low

313 BAODs. Overall, the BAOD map clearly reveals the most heavily polluted region as a
314 hotspot.
315 The surface reflectance was estimated from the minimum TOA reflectance, after
316 correcting for atmospheric and BAOD effects. For details of the atmospheric
317 correction, see Kim et al. (2014).
318
319 **3.3. Integration of Aerosol model**
320
321 The calculated TOA reflectance from RTM simulations is affected by the
322 concentration, particle size/shape and scattering properties of aerosol. Consequently,
323 an increase in the SSA of the particle correlates positively with TOA reflectance for
324 the same AOD. The use of a well-defined aerosol model to generate the LUT is
325 therefore crucial to obtain accurate AOD values from the inversion method. Although
326 spatial variation of the aerosol characteristics shown in Figure 2 was not taken into
327 account, a regionally integrated aerosol model over the area of interest suggest typical
328 properties from these areas, since the geostationary MI steadily observes the same
329 field of view from a fixed location. In this study, the aerosol models were obtained
330 from a seasonal average of AERONET inversion datasets over East Asia. There are
331 two groups of inversion datasets applied to examine the effect of the DRAGON-NE
332 Asia campaign on the retrieval accuracy of aerosol. The first datasets were compiled
333 from 18 AERONET sites from 1999 to 2010, with total 4898 data points as used by
334 Kim et al. (2014). This group was named as the ‘original’ dataset, where the name and
335 location of these sites are represented by italic type. The full list shown by normal
336 character in Table 1 summarizes the sites used to construct the ‘new’ data set as
337 described in Section 2.1.

338 The new group includes 40 additional AERONET sites and extends the measurement
339 period by up to 2 years (2011 ~ 2012) including the campaign. The greater quantity of
340 data, from the increased number of sites for the extended measurement periods,
341 allows us to optimize the aerosol model for the region of interest.
342 To compare the effects of the temporal extension and spatially more dense
343 measurements, the integrated AOPs for each case are presented in Table 2. In the
344 table, AOPs considered to calculate LUT for MAM (March, April, and May) season
345 were listed for each AOD bin in order of SSA, refractive index, effective radius and
346 standard deviation of volume size distribution, and the number of integrated data. To
347 consider the change in AOP with respect to AOD suggested by Levy et al. (2007), the
348 AOPs were categorized for six AOD bins. The bins are categorized by 0.0-0.3, 0.3-0.6,
349 0.6-1.0, 1.0-1.4, 1.4-1.8, and 1.8-3.0, and the median values of each AOD bin are
350 shown in Table 2. Though AERONET inversion data provide four spectral SSAs at
351 440, 675, 870, and 1020 nm, the values at 675 nm were analysed considering the
352 spectral range of MI visible channel. For the LUT calculation, however, wavelength
353 dependence of the refractive index was obtained from the AERONET retrieval and
354 applied. Based on the wavelength dependence, the AOD was retrieved at 550 nm. The
355 total average and standard deviation of the SSA for the 'original' group (Table 2(a))
356 was 0.92 and 0.035, respectively. The SSA ranged between 0.911 and 0.925 in order
357 of AOD. Accordingly, real part of the refractive index showed positive correlation
358 with the AOD. The increase of AOD caused the increase of effective radius and
359 standard deviation of fine mode size distribution, too. With the quality criteria of the
360 inversion products, the number of data points was significantly low for the low AOD
361 bin. The number of data was also decreased with the increasing AOD. In Table 2 (b),
362 the AOPs obtained from the temporally extended datasets from the same sites were

363 listed. A slight increase of the effective radius for coarse mode particle was found for
364 the low AOD cases in accordance with the increase of the number of data. When the
365 dataset from the DRAGON-NE Asia campaign, and a few additional sites in China
366 not included in the original study, were applied, all of AOD bins showed increased
367 SSA by more than 0.005, and the average value was 0.93 ± 0.035. The larger dataset
368 resulted in SSA by about 1%, though the variation is lower than the standard
369 deviation of SSA. The increase in SSA may also be due to a temporal change in SSA
370 which was suggested in Lyapustin et al. (2011a). The previous study showed
371 increases in SSA in eastern China from 2000 to 2010 by about 0.02 at 470 nm. The
372 imaginary part of the refractive index was generally decreased, and the decrease was
373 more significant for low AOD condition than high AOD condition. Meanwhile, the
374 increasing effective radius of coarse particle was also found. Figure 5 shows the
375 volume size distribution analysed from the original (Figure 5a) and the new data
376 (Figure 5b) group for each AOD bin. In general, the coarse mode particles of a bi-
377 modal log-normal size distribution tend to dominate due to sporadic dust events [e.g.
378 Lee at al., 2010b]. With the increase in AOD, the mode radius of fine particles is
379 increased, while that of coarse particles is decreased [Levy et al., 2007a]. The
380 effective radius and standard deviation for fine and coarse mode were listed in Table
381 2(a) and (c).
382 Using aerosol models derived from both the original and new datasets, LUTs were
383 calculated by using the 6SV (Second Simulation of a Satellite Signal in the Solar
384 Spectrum–Vector) RTM (Vermote et al., 1997; Kotchenova et al., 2006; Kotchenova
385 and Vermote, 2007). In addition to measurement geometry (i.e. solar zenith angle,
386 viewing zenith angle, and relative azimuth angle), the surface reflectance, aerosol

387 model, and AOD were provided as input variables to calculate the LUTs. Surface
388 elevation was also included to increase the accuracy of Rayleigh scattering correction.
389 As mentioned above, the AOD is retrieved by comparing measured and calculated
390 TOA reflectance for a given set of measurement condition. The values in the LUTs
391 were linearly interpolated with the values in the neighbouring bins because the
392 calculation of TOA reflectance is performed as a function of several input variables.
393 To test the effects of the changes in aerosol models, the AODs were respectively
394 derived by using the original and the new LUTs.
395
396 **3.4. Sensitivity to assumed aerosol optical properties**
397
398 To estimate the accuracy of retrievals from the inversion of the single channel
399 algorithm, and to understand its sensitivity to uncertainty in the assumed SSA, a
400 reference test was performed. In this test, the TOA reflectance, was analysed within a
401 ±4% variation in SSA relative to the reference condition, from simulations using the
402 RTM for four different reference conditions of both AOD and SSA with assumed
403 geometries. The 4% variation covers the standard deviation of 0.035 for the integrated
404 SSA of 0.92 mentioned in section 3.3. In the simulation, the surface reflectance was
405 assumed to be 0.05 and 0.10, and the scattering angle was varied from 135.7° to 173.2°
406 with respect to the geostationary measurement conditions. The surface elevation was
407 at sea level, and cloud-free conditions were assumed. The retrieved AOD from the
408 simulated reflectance was then compared with the assumed reference AOD value.
409 Because the AOD was retrieved from the simulated TOA reflectance by assuming the
410 reference SSA, the ±4% variation in SSA cause an error in AOD. The results for the
411 comparison between the reference value and retrieved AODs for each simulated

412 reflectance are shown in Figure 6. The case with zero SSA error indicates that the
413 assumed SSA for the retrieval was the same as the reference SSA. In other cases, the
414 positive error in SSA indicates that the SSA used to calculate the LUT was
415 overestimated when compared with the reference value. The errors in AOD and SSA
416 were calculated as follows:
417
418 $$\text{AOD error [\%]} = [(\text{retrieved AOD} - \text{reference AOD})/\text{reference AOD}]\cdot 100$$
419
420 $$\text{SSA error [\%]} = [(\text{assumed SSA} - \text{reference SSA})/\text{reference SSA}]\cdot 100$$
421
422 Strong negative correlation was found between the errors in SSA and AOD. The error
423 in SSA was negatively correlated with error in AOD, and thus the overestimation of
424 SSA leads to an underestimation of AOD. In terms of the absolute value of AOD error,
425 the effects of the positive and negative errors in SSA are symmetric in general, though
426 the effect of the negative error in SSA is slightly greater. The effect of assumed errors
427 in SSA is more significant in scenarios with higher AOD. The SSA error of ±3%
428 results in an AOD error of -18.70% (-0.03, an absolute difference) and +20.34%
429 (+0.03), respectively, when the reference AOD is 0.15 and the surface reflectance is
430 0.05. The range of error is increased when the reference AOD is higher, with retrieval
431 errors of -20.03% (-0.24) and +23.31% (+0.28) caused by a ±3% SSA error when the
432 reference AOD is 1.20.
433 The error in AOD also increases with the increase of assumed surface reflectance
434 relative to true reflectance. When the surface reflectance is increased from 0.05 to
435 0.10, the errors in the reference AOD of 0.15 ranged between -35% (-0.05) and 36%
436 (+0.05). The increase of effect of the SSA assumption was related with the one-to-one

correlation between the ‘critical reflectance’ and SSA reflectance (Castanho et al., 2008; Fraser and Kaufman, 1985). Whereas the increase of aerosol contributes to the increase of TOA reflectance over dark surface, the increase of AOD reduces the TOA reflectance by shielding the upwelling reflectance from bright surface. There exist, therefore, the surface reflectance at which the positive and negative contributions of aerosol to the TOA reflectance are cancelled out, then the surface reflectance is known as the critical reflectance. In consideration of the positive relationship between the critical reflectance and SSA, the sensitivity to SSA assumption of the AOD retrieval can be increased near the critical reflectance.

3.5. Uncertainty of AOD retrieval

Various uncertainties result in error in AOD retrieved as the algorithm is based on a single channel, where most dominant uncertainties come from estimating surface reflectance and assumed aerosol model. To investigate the retrieval error, several sensitivity tests were conducted. The effects of linear inversion error, assumptions of BAOD, aerosol model and surface elevation were estimated in a quantitative manner in addition to aerosol model error shown in Figure 6.

The LUT approach has been widely used to take aerosol information from satellite measurement by reducing operation time. In LUT approach, the calculated value is interpolated linearly from the neighboring bins for geometry, AOD, surface reflectance, and elevation. Thus, the number of entries for LUT calculation must be selected carefully to save operation time and maintain retrieval accuracy at the same time. LUT applied in this study presents TOA reflectance calculated as a function of

461 geometrical angles of sun and satellite with 10° interval, and surface reflectance with
462 0.1 intervals. As long as the LUT approach is applied to retrieval algorithm, the linear
463 interpolation of TOA reflectance between each bin leads to the inversion error. Figure
464 7(a) and (b) show the percentage difference between retrieved and reference AODs in
465 terms of scattering angle, surface reflectance, and AOD condition. Two different
466 AODs of 0.15 and 1.20 were applied to calculate the reference reflectance with two
467 surface reflectances of 0.05 and 0.10, and solar zenith angles ranging from 0° to 57°
468 by 3° interval. The satellite zenith and azimuth angle were assumed as 10° and 40°,
469 respectively. In Figure 7(a, b), the percentage errors increase by increasing difference
470 between the reference condition and LUT bin in terms of both scattering angle and
471 surface reflectance. The inversion error varied from 0 to 8%, which mainly increased
472 with the increase of scattering angle, and decreased with the increase of AOD. In the
473 figure, the solid lines represent the inversion error arisen solely by the angle
474 interpolation in interval of 0.1 for the surface reflectance in LUT. The dashed lines
475 representing the inversion error for the surface reflectance of 0.05 shows that the
476 assumption about linearity between bins of surface reflectance increased the error
477 negatively.
478 In the estimation of surface reflectance, the BAOD correction was applied to consider
479 continuous emission of air pollutant over East Asia. However, the BAOD estimated
480 from MODIS products contains retrieval uncertainty of the dark target algorithm. As
481 mentioned above, the expected error range of MODIS AOD is ±(0.05 + 15%). The
482 BAOD is very low in general, and thus the expected error range can be over ±100%
483 when the BAOD is lower than 0.05. According to a sensitivity test, the ±100% error
484 in the BAOD of 0.05 led to 7% error in surface reflectance of 0.05 and 11% error in
485 AOD of 0.45. The effects of BAOD error in surface reflectance and AOD are shown

in Figure 7(c) and (d), respectively, under the conditions of BAOD of 0.15, three surface reflectance of 0.05, 0.10, and 0.15, and three AODs of 0.45, 0.80, and 1.20. In general, the underestimation of the BAOD leads to the overestimation of the surface reflectance. The -100 % error in the BAOD assumption caused 5.6 % overestimation of surface reflectance when the surface reflectance was 0.1. Meanwhile, the 5 % error in surface reflectance led to 25.56 % underestimation of the AOD when the reference AOD and surface reflectance was 0.45 and 0.10, respectively. The uncertainty was decreased with the increase of surface reflectance, and the sensitivity to the error in surface reflectance was more significant for the low AOD condition than the high AOD. In this test, the inversion error was avoided by using reference reflectance calculated under the condition of LUT bins.

Lastly, the effect of assumption in surface elevation was analyzed, as shown in Figure 7(e). The assumption of surface elevation is linked with the Rayleigh scattering correction. The underestimation of surface elevation leads to the overestimation of atmospheric pressure, thus the over-correction of the Rayleigh scattering which eventually results in the overestimation of surface reflectance, thus the underestimation of the AOD. The sensitivity was tested for an elevation of 1 km, two AODs of 0.15 and 0.80, and surface reflectances of 0.10. The ±0.5 km errors in surface elevation resulted in +9.63% and -10.56% errors in AOD when the reference condition was assumed as the AOD of 0.15. The increasing AOD significantly reduced sensitivity to the uncertainty, and ± 0.5 km error led +1.30 % and –1.43 % when the AOD was 0.80. The dependence on surface reflectance and elevation were not significant.

From the uncertainty tests, the largest uncertainty was found in the aerosol model assumption by about 30 % although the effect of each uncertainty was changed by condition of AOD, surface reflectance, and sun-satellite geometry.

4. Results and validation

4.1. Comparison with MODIS AOD

The greatest advantage of geostationary measurements is the availability of more cloud-free observations by continuous measurements at high temporal resolution. Besides, The AOD derived from geostationary satellite measurements can minimize the uncertainty caused by the different and limited sampling of polar-orbiting-satellite in the trend estimation (Yoon et al., 2014). Figure 8 shows examples of retrieved AOD from the geostationary measurements from MI, using the single channel algorithm. The RGB images, obtained from GOCI onboard the same platform measured at 01:16, 02:16, 03:16, 04:16, 05:16 and 06:16 UTC on April 27, 2012, show dust flow from the Shandong Peninsula to the northern Korean Peninsula. Similarly, the images of retrieved AOD show values greater than 1.0 in the dust plume, in contrast to the values lower than 0.4 over other regions. Compared with the MODIS AOD, the retrieved AOD over dusty regions are generally higher, though the distribution of MI AOD is spatially well matched over non-dusty regions. Spatially averaged value of the MI AOD in dusty region [110°E-125°E, 35°N -40°N] decreased steadily from 2.67 at 00 UTC to 1.69 at 07 UTC, and the minimum value of 1.43 was found at 03:30 UTC. Meanwhile, the spatial mean values of AOD obtained respectively from the MODIS TERRA and AQUA measurements were 1.11 at 03:55

534 UTC and 1.18 at 05:15 UTC. In the Figure 8, the AOD images of TERRA and AQUA
535 represent the measurements between 00 UTC to 05 UTC, and between 02 UTC to 06
536 UTC, respectively.
537 The results from MI also show the transport and concentration of aerosol in 30-min
538 interval, while the MODIS product can provide only two images per day. The map of
539 MI AOD in hourly intervals shows that the high concentration of aerosol was mostly
540 observed over northern China and the Yellow Sea before 0300 UTC, with the dust
541 plume extending to the East Sea across the northern Korean Peninsula. We can
542 deduce from the change in the dust plume that the wind field changed straight flow
543 from southwest to northeast in the morning to wave pattern, following a low pressure
544 system located in Manchuria. Neither the dark target algorithm of MODIS nor the
545 single channel algorithm of MI could retrieve AOD over regions of brighter surfaces,
546 due to the low sensitivity of the aerosol compared with the surface. However, unlike
547 the MI retrieval, part of the dust scene over the ocean was missed in the MODIS
548 retrieval due to sun-glint masking.
549
550 **4.2. Comparison with AERONET: DRAGON-Asia**
551
552 For quantitative validation, the retrieved AODs were compared with the measured
553 values from the 39 AERONET sun-photometer sites in Korea and Japan. To
554 investigate the effect of the new aerosol model as an input parameter to calculate the
555 LUTs, the results of the original and new AOD retrievals were compared respectively,
556 and the comparisons were shown in Figure 9. The measured AODs from all of the
557 numbered DRAGON-Asia sites listed in Table 1 were used in the comparison shown
558 in the top panel. In the lower panel, part of the AERONET AOD was used as a

validation group to test the consistency of the algorithm and to validate the retrieval accuracy. The data from the validation group were not included in the AOP analysis due to a lack of inversion datasets. The comparison results are shown in the bottom panel of Figure 9. The left and right panels show evaluations of the original and new AOD, respectively.

Using the original aerosol model, the retrieved AODs agree very well with the linear regression as follows:

$$\tau_{\text{MI [original LUT]}} = 1.08\tau_{\text{DRAGON-Asia}} - 0.08,\ \text{RMSE} = 0.18,\ r = 0.87$$

Although the Pearson coefficient of 0.87 indicates a significant correlation, the regression slope indicates that the retrieved AOD is overestimated by 8% compared with the AERONET value. Comparison with the validation group, however, shows a tendency to systematic underestimation with a slope of 1.01 and y-offset of -0.05.

By applying the new aerosol model, the regression slope was improved to 1.00, although other measures remained similar:

$$\tau_{\text{MI [new LUT]}} = 1.00\tau_{\text{DRAGON-Asia}} - 0.07,\ \text{RMSE} = 0.17,\ r = 0.85$$

In Section 3.4, the analysis of the retrieval sensitivity to the SSA assumption showed that the underestimation of the SSA in the aerosol model results in the overestimation of AOD. Thus, the overestimation of the original AOD suggests that the radiative absorptivity of the aerosol during MAM was slightly underestimated prior to the campaign. According to Figure 6, a 1% underestimation of SSA can result in overestimation of AOD by up to 7%. The uncertainty can vary with measurement

584 geometry, AOD, or surface reflectance. Therefore, to a large degree, the 8% decrease
585 in AOD can be explained by a 1.1% increase in SSA in the new aerosol model during
586 MAM. The large RMSE and the underestimation for the validation group, however,
587 are attributed to the spatial and temporal variation in AOPs, which cannot be
588 standardized by the single aerosol model. Moreover, the change of aerosol model
589 results in a decrease of percentage of the comparison data within 30% difference
590 range from 79.15% to 77.30%. In terms of the comparison of the validation group, the
591 regression slope was decreased from 1.01 to 0.93 though the comparison still shows
592 strong correlation between the retrieved and measured AOD. As long as a single
593 aerosol model is applied, the spatial and temporal variations of aerosol properties are
594 the largest uncertainty of the AOD retrieval algorithm. When the difference between
595 assumed and actual SSA become higher than 3%, the retrieval error exceed 30%. The
596 degradation of the comparison statistics shows the limitation of the single channel
597 algorithm. The uncertainties in estimation of surface reflectance and assumption of
598 linearity between LUT bins have effects on the accuracy of low AOD as described in
599 section 3.5. The sensitivity tests showed that the effects of each retrieval uncertainty
600 depend on the condition of AOD. For the condition of low AOD, the effect of aerosol
601 model assumption to the retrieval uncertainty in AOD is significantly lower than the
602 effects of surface reflectance estimation. However, insufficient number of inversion
603 data for an AOD bin between 0.0 and 0.3, where the AOD is lower than the criteria of
604 quality assurance of 0.4 (440 nm), increases the uncertainty in the assumption of
605 aerosol model for the condition of low AOD. Consequently, it was found that the
606 validation statistics for low AOD (< 0.4 at 550 nm) were significantly lower than that
607 for high AOD. While the correlation coefficient and regression slope of the low AOD
608 comparison was 0.49 and 0.35, those for high AOD condition was 0.78 and 0.86. The

609 ratio of the low AOD to the total comparison data set was 41.72%. To show the
610 retrieval accuracy for each campaign site, the Taylor diagram (Taylor, 2001) is shown
611 in Figure 10. This diagram summarizes how closely a set of retrievals matches
612 observations in terms of r, RMSE, and standard deviation. The polar angle of the
613 point from the x-axis indicates the correlation coefficient, and the radial distance
614 represents the normalized standard deviation, which in this case describes the ratio of
615 the standard deviation of the retrieved MI AOD to that of the AERONET (Yoon et al.,
616 2014) values. The distance between the symbol and the dashed arc, which represents
617 the standard deviation of the AERONET value, shows the similarity of the amplitude
618 of their variations; a radial distance of >1 indicates that the standard deviation of the
619 MI AOD is greater than that of AERONET. On the other hand, the RMSE between
620 the MI and AERONET AODs is proportional to the distance to the point on the x-axis
621 identified as “AERONET”, marked with a dotted arc. Consequently, the decrease in
622 distance between the “AERONET” point and the position of the symbol indicates an
623 increase in similarity between the retrieved and measured AODs. The normalized
624 standard deviations of retrieved AOD generally range from 1 to 1.5, except for the
625 Kohriyama (site number 12) and Matsue (site number 19) in Japan. In spite of the
626 high correlation coefficients of 0.85 and 0.78 at the sites, the high regression slopes of
627 1.58 and 1.35 suggest that the radiative absorptivity was underestimated in this region,
628 and thus the AOD was significantly overestimated in the case of high-AOD
629 conditions. The large negative y-intercepts of -0.12 and -0.25 could be caused by the
630 underestimation of AOD following an overestimation of BAOD in the case of low-
631 AOD conditions.
632 The comparison statistics of the original and new AOD, plotted in the Taylor diagram,
633 are also listed in Tables 3 and 4, respectively. The correlation coefficients obtained

634 from the 39 DRAGON sites range from 0.66 to 0.95 and the average was 0.84 when
635 the original aerosol model was applied. The maximum value was found at Anmyeon
636 (site number 3) and Kunsan_NU (National University) in Korea, and the minimum
637 value of 0.66 was found at Nishi-Harima (site number 25) in Japan. The Anmyeon
638 site was located in a rural area near ocean to monitor background condition of
639 atmosphere (e.g., Kim et al., 2007), and thus the dark surface contributes to reduce the
640 uncertainty in AOD retrieval. The Kunsan-NU site, as with the Anmyeon site, was
641 surrounded by mountain, reservoir, and rural area. Meanwhile, the Nishi-Harima site
642 was located on the top of Mount Onade (435.9 meters altitude, Nishi-Harima
643 Astronomical Observatory) among trees, and thus the uncertainty caused during
644 surface correction can be reduced, also. However, the comparison statistics showed
645 systematic underestimation of the AODs by regression slope of 0.86 and y-intercept
646 of -0.06. To compare the difference between the AOD correlations for each sites,
647 temporal variation of the AODs obtained from MI and AERONET measurements
648 were represented in Figure 11. In Figure 11, the AOD variations for the four
649 aforementioned sites were shown in order of (a) Anmyeon, (b) Kunsan_NU, (c)
650 Kohriyama, and (d) Nishi-Harima site. The red boxes and black circles, which
651 indicate the MI AOD and the AERONET value, were well matched at (a) Anmyeon
652 and (b) Kunsan-NU with good correlation statistics. The vertical distribution of
653 symbols for each day represents diurnal variation of AOD, and the variations were
654 also highly correlated regardless of time. The temporal variations showed AOD
655 increase during the period from 1 to 15 May at both sites. In other two sites in Japan,
656 Kohriyama and Nishi-Harima, any temporal pattern cannot be found because of the
657 low number of comparison data, though the variation of MI AOD was closely related
658 with the AERONET value. A notable thing in the comparison was the low number of

659 data. Table 3 showed that most of Japanese site (excepting Fukue) has lower
660 comparison data than the sites of Korean, and the low number trend was related with
661 frequency of the direct measurements of sun-photometer in Japan sites. While the
662 total number of direct AOD products in level2.0 dataset ranged between 99 and 3630
663 in Japan, the number ranged from 1296 to 5191 in Korea. The difference in data
664 counts indicates that there was frequent rain and cloud event over Japan, to result in
665 uncertainty in the AOD retrieval in the Japan including Koriyama and Nishi-Harima
666 site. However, reason of the significant underestimation trend of the MI AOD at
667 Nishi-Harima is not clear yet.
668 Excluding Fukue_2 site which has low comparison data of only 4, the regression
669 slopes at 32 AERONET sites were higher than 1.0, and the values at 9 sites exceeded
670 1.2. As well as the Kohriyama and the Matsue sites, the comparison results for all but
671 three sites (2, 30, and 32) show negative y-intercepts between –0.003 and –0.25. As
672 with the improved correlation seen in the scatter plot, the Taylor diagram and
673 regression statistics listed in Table 4 also show improvements in retrieval accuracy at
674 each site. The distances between the data point and the "AERONET" value at each
675 site were generally reduced, especially at Tsukuba (site number 32). At this site, the
676 systematic overestimation was significantly reduced by applying the new aerosol
677 model, also leading to an improved correlation coefficient. The regression slope over
678 all sites was decreased by about 0.08, while the y-intercept was changed within a
679 range from -0.03 to 0.06, in accordance with the increased SSA in the new aerosol
680 model. Whereas most of the comparisons were improved by the decrease in the slope,
681 some sites (11, 21, 25, 26, 28 and 36) show a better result using the original aerosol
682 model in terms of the regression slope. The change in correlation coefficient and
683 RMSE was not significant.

5. Summary

A single channel algorithm was used to retrieve AOD over East Asia by adopting a new aerosol model, derived from data from the mesoscale network measurement campaign deploying sun-sky radiometers, DRAGON-NE Asia 2012. The campaign was performed during MAM 2012 to improve our understanding of the AOPs in high spatial scale over well-known aerosol source regions where aerosol loading is affected by both desert emissions and industrial pollutants. In addition, the direct solar measurements of spectral AOD undertaken during the campaign were used to improve the satellite-based aerosol retrieval algorithm by providing a dataset for validation.

The accuracy of the single channel algorithm is strongly affected by the surface reflectance estimation and the assumed aerosol model. To estimate the surface reflectance, a minimum reflectance method was applied, and the BAOD was used to correct for the persistent background aerosol levels over East Asia. The BAOD was obtained by using the MODIS standard AOD product from 2006 to 2012. With respect to aerosol model selection, however, the single channel algorithm was limited by a lack of spectral information. For this reason, the aerosol model was integrated from a seasonally sorted inversion dataset taking into account the monsoon climate over the region, which was used to calculate LUT. To overcome the limitations of the retrieval accuracy related to the limitation in aerosol type selection, it was important to optimize the aerosol model. The AOPs were obtained from two AERONET inversion data groups to understand the effects of assumptions in the aerosol model. The original AOPs were constructed from the inversion dataset provided by 13

AERONET sites over East Asia before 2011, while the new AOPs were modified using data from an increased number of measurement sites, as well as additional data from the original sites. The obtained AOPs show that the denser deployment of measurement sites has a greater effect on the AOPs than the extended periods of measurement in terms of refractive index. The increase of effective radius of coarse particle distribution as found also. This increase in spatial resolution resulted in an increase of SSA by ~1.1% during MAM, which was expected to lead to a decrease in AOD.

According to the sensitivity test, the error in the retrieved AOD varied from -19% to +20%, in proportion with the assumed SSA error of ±3% in the aerosol model, for a scenario with reference AOD value of 0.15 and the surface reflectance of 0.05. The uncertainty in retrieved AOD due to the assumed SSA error was increased at greater values of AOD, and ranged between -20% and +23% when the reference AOD value was 1.20. In short, the overestimation of SSA in the aerosol model results in the underestimation of AOD, and assumed errors in SSA have a greater effect at higher values of AOD. Considering the relationship between surface reflectance and the uncertainty, the retrieval error in real measurements could be larger than the suggested value when the surface reflectance is near the critical reflectance. In the meantime, the error in surface reflectance shows larger effects in the accuracy of low AOD than the error in SSA.

The qualitative comparison between AODs retrieved from MODIS and MI showed a reasonably high correlation. The MI AOD showed the capability to track the dust plume crossing from the Shandong Peninsula to the northern Korean Peninsula by taking advantage of geostationary measurements, whereas the MODIS AOD provided two AOD maps during a single day by using both Terra and Aqua. AODs retrieved

with both the original and new aerosol model showed a good correlation with sun-photometer data from the DRAGON-Asia campaign. The correlation coefficient and the RMSE were slightly changed from 0.87 to 0.85 and 0.18 to 0.17, respectively, by applying the new aerosol model. Increased SSA values in the new aerosol model resolved problems with AOD being overestimated, and the regression slope was decreased from 1.08 to 1.00. A comparison for each campaign site also showed that the statistics of the correlation were generally improved. For some regions, however, changes in the aerosol model led to underestimation of the AOD.

As shown here, the use of a fixed aerosol model is an important issue in a single channel algorithm. Similarly, the application of a well-defined model for each assumed aerosol type is important to obtain accurate results from a multi-channel algorithm. According to a study with the GOCI multi-channel algorithm (Choi et al., accepted), however, the effects of applying the DRAGON-Asia dataset were less significant, in other words less dependent on the aerosol model assumed. The GOCI algorithm categorizes 26 aerosol models according to FMF at 550 nm and SSA at 440 nm, and selects an optimized aerosol type at each measured pixel and time. The accuracy of the BAOD is another important issue when using the minimum reflectance method to retrieve AOD, because overestimation of the BAOD results in a systematic underestimation of the AOD. The dense measurements of the AERONET sun-photometer network can be used to optimize the BAOD at higher resolution, though the network cannot cover the whole field of view of the satellite measurement. Furthermore, an improved correction for cloud masking is required to reduce noise in the retrieval.

Acknowledgements

We thank the principal investigators and their staff for establishing and maintaining the AERONET sites used in this investigation. We also gratefully acknowledge the PI and staffs of DRAGON-NE Asia campaign for theirs effort. This research was supported by the GEMS program of the Ministry of Environment, Korea, and the Eco Innovation Program of KEITI (2012000160002). This research was partially supported by the Brain Korea 21 Plus (J. Kim and M. Kim).

References

Bevan, S. L., North, P. R. J., Los, S. O., and Grey, W. M. F.: A global dataset of atmospheric aerosol optical depth and surface reflectance from AATSR, Remote Sens Environ, 116, 199-210, 10.1016/j.rse.2011.05.024, 2012.

Castanho, A. D. D. A., Martins, J. V., and Artaxo, P.: MODIS aerosol optical depth Retrievals with high spatial resolution over an urban area using the critical reflectance, J Geophys Res-Atmos, 113, Artn D02201 Doi 10.1029/2007jd008751, 2008.

Choi, M., Kim, J., Lee, j., Kim, M., Park, Y.-J., Jeong, U., Kim, W., Holben, B., Eck, T.F., Lim, J. H., and Song, C. K.: GOCI Yonsei Aerosol Retrieval (YAER) Algorithm and Validation During DRAGON-NE Asia 2012 Campaign, Atmos. Meas. Tech. Discuss., accepted, 2015

Deroubaix, A., Martiny, N., Chiapello, I., and Marticorena, B.: Suitability of OMI aerosol index to reflect mineral dust surface conditions: Preliminary application for studying the link with meningitis epidemics in the sahel, Remote Sens Environ, 133, 116-127, DOI 10.1016/j.rse.2013.02.009, 2013.

784 Dubovik, O., and King, M. D.: A flexible inversion algorithm for retrieval of aerosol
785 optical properties from Sun and sky radiance measurements, J Geophys
786 Res-Atmos, 105, 20673-20696, Doi 10.1029/2000jd900282, 2000.
787 Dubovik, O., Smirnov, A., Holben, B. N., King, M. D., Kaufman, Y. J., Eck, T. F.,
788 and Slutsker, I.: Accuracy assessments of aerosol optical properties
789 retrieved from Aerosol Robotic Network (AERONET) Sun and sky
790 radiance measurements, J Geophys Res-Atmos, 105, 9791-9806, Doi
791 10.1029/2000jd900040, 2000.
792 Dubovik, O., Holben, B., Eck, T. F., Smirnov, A., Kaufman, Y. J., King, M. D., Tanre,
793 D., and Slutsker, I.: Variability of absorption and optical properties of key
794 aerosol types observed in worldwide locations, J Atmos Sci, 59, 590-608,
795 Doi 10.1175/1520-0469(2002)059<0590:Voaaop>2.0.Co;2, 2002.
796 Eck, T. F., Holben, B. N., Reid, J. S., Dubovik, O., Smirnov, A., O'Neill, N. T.,
797 Slutsker, I., and Kinne, S.: Wavelength dependence of the optical depth of
798 biomass burning, urban, and desert dust aerosols, J Geophys Res-Atmos,
799 104, 31333-31349, Doi 10.1029/1999jd900923, 1999.
800 Fraser, R. S., and Kaufman, Y. J.: The relative importance of aerosol scattering and
801 absorption in remote-sensing, IEEE T Geosci Remote, 23, 625-633, Doi
802 10.1109/Tgrs.1985.289380, 1985.
803 Frey, R. A., Ackerman, S. A., Liu, Y. H., Strabala, K. I., Zhang, H., Key, J. R., and
804 Wang, X. G.: Cloud detection with MODIS. Part I: Improvements in the
805 MODIS cloud mask for collection 5, J Atmos Ocean Tech, 25, 1057-1072,
806 10.1175/2008jtecha1052.1, 2008.
807 Grey, W. M. F., North, P. R. J., Los, S. O., and Mitchell, R. M.: Aerosol optical depth
808 and land surface reflectance from Multiangle AATSR measurements:

809 Global validation and intersensor comparisons, Ieee T Geosci Remote, 44,
810 2184-2197, 10.1109/Tgrs.2006.872079, 2006.
811 Holben, B. N., Eck, T. F., Slutsker, I., Tanre, D., Buis, J. P., Setzer, A., Vermote, E.,
812 Reagan, J. A., Kaufman, Y. J., Nakajima, T., Lavenu, F., Jankowiak, I., and
813 Smirnov, A.: Aeronet - a federated instrument network and data archive for
814 aerosol characterization, Remote Sens Environ, 66, 1-16, Doi
815 10.1016/S0034-4257(98)00031-5, 1998.
816 Holben, B. N., Tanre, D., Smirnov, A., Eck, T. F., Slutsker, I., Abuhassan, N.,
817 Newcomb, W. W., Schafer, J. S., Chatenet, B., Lavenu, F., Kaufman, Y. J.,
818 Castle, J. V., Setzer, A., Markham, B., Clark, D., Frouin, R., Halthore, R.,
819 Karneli, A., O'Neill, N. T., Pietras, C., Pinker, R. T., Voss, K., and Zibordi,
820 G.: An emerging ground-based aerosol climatology: Aerosol optical depth
821 from AERONET, J Geophys Res-Atmos, 106, 12067-12097, Doi
822 10.1029/2001jd900014, 2001.
823 Hsu, N. C., Tsay, S. C., King, M. D., and Herman, J. R.: Aerosol properties over
824 bright-reflecting source regions, IEEE T Geosci Remote, 42, 557-569, Doi
825 10.1109/Tgrs.2004.824067, 2004.
826 Huebert, B. J., Bates, T., Russell, P. B., Shi, G. Y., Kim, Y. J., Kawamura, K.,
827 Carmichael, G., and Nakajima, T.: An overview of ACE-Asia: Strategies
828 for quantifying the relationships between Asian aerosols and their climatic
829 impacts, J Geophys Res-Atmos, 108, Artn 8633
830 Kahn, R. A., Gaitley, B. J., Garay, M. J., Diner, D. J., Eck, T. F., Smirnov, A., and
831 Holben, B. N.: Multiangle Imaging SpectroRadiometer global aerosol
832 product assessment by comparison with the Aerosol Robotic Network, J
833 Geophys Res-Atmos, 115, Artn D2320910.1029/2010jd014601, 2010.

834 Kim, J., Lee, J., Lee, H. C., Higurashi, A., Takemura, T., and Song, C. H.:
835 Consistency of the aerosol type classification from satellite remote sensing
836 during the atmospheric brown cloud-east Asia regional experiment
837 campaign, J Geophys Res-Atmos, 112, Artn D22s33Doi
838 10.1029/2006jd008201, 2007.
839 Kim, J., Yoon, J. M., Ahn, M. H., Sohn, B. J., and Lim, H. S.: Retrieving aerosol
840 optical depth using visible and mid-IR channels from geostationary satellite
841 MTSAT-1R, Int J Remote Sens, 29, 6181-6192, Doi
842 10.1080/01431160802175553, 2008.
843 Kim, M., Kim, J., Wong, M. S., Yoon, J., Lee, J., Wu, D., Chan, P. W., Nichol, J. E.,
844 Chung, C.-Y. C., and Ou, M.-L.: Improvement of aerosol optical depth
845 retrieval over Hong Kong from a geostationary meteorological satellite
846 using critical reflectance with background optical depth correction, Remote
847 Sens Environ, 142, 176-187, 2014.
848 Knapp, K. R., Vonder Haar, T. H., and Kaufman, Y. J.: Aerosol optical depth retrieval
849 from goes-8: Uncertainty study and retrieval validation over South America,
850 J Geophys Res-Atmos, 107, Artn 4055Doi 10.1029/2001jd000505, 2002.
851 Knapp, K. R., Frouin, R., Kondragunta, S., and Prados, A.: Toward aerosol optical
852 depth retrievals over land from GOES visible radiances: Determining
853 surface reflectance, Int J Remote Sens, 26, 4097-4116, Doi
854 10.1080/0143116050500099329, 2005.
855 Kotchenova, S. Y., Vermote, E. F., Matarrese, R., and Klemm, F. J.: Validation of a
856 vector version of the 6S radiative transfer code for atmospheric correction
857 of satellite data. Part i: Path radiance, Applied optics, 45, 6762-6774, Doi
858 10.1364/Ao.45.006762, 2006.

859 Kotchenova, S. Y., and Vermote, E. F.: Validation of a vector version of the 6S
860 radiative transfer code for atmospheric correction of satellite data. Part ii.
861 Homogeneous Lambertian and anisotropic surfaces, Applied optics, 46,
862 4455-4464, Doi 10.1364/Ao.46.004455, 2007.
863 Lee, J., Kim, J., Song, C. H., Kim, S. B., Chun, Y., Sohn, B. J., and Holben, B. N.:
864 Characteristics of aerosol types from AERONET sunphotometer
865 measurements, Atmos Environ, 44, 3110-3117, DOI
866 10.1016/j.atmosenv.2010.05.035, 2010a.
867 Lee, J., Kim, J., Song, C. H., Ryu, J. H., Ahn, Y. H., and Song, C. K.: Algorithm for
868 retrieval of aerosol optical properties over the ocean from the Geostationary
869 Ocean Color Imager, Remote Sens Environ, 114, 1077-1088, DOI
870 10.1016/j.rse.2009.12.021, 2010b.
871 Lee, J., Kim, J., Yang, P., and Hsu, N. C.: Improvement of aerosol optical depth
872 retrieval from MODIS spectral reflectance over the global ocean using new
873 aerosol models archived from AERONET inversion data and tri-axial
874 ellipsoidal dust database, Atmos Chem Phys, 12, 7087-7102, DOI
875 10.5194/acp-12-7087-2012, 2012.
876 Levy, R. C., Remer, L. A., and Dubovik, O.: Global aerosol optical properties and
877 application to Moderate Resolution Imaging Spectroradiometer aerosol
878 retrieval over land, J Geophys Res-Atmos, 112, Artn
879 D1321010.1029/2006jd007815, 2007a.
880 Levy, R. C., Remer, L. A., Mattoo, S., Vermote, E. F., and Kaufman, Y. J.: Second-
881 generation operational algorithm: Retrieval of aerosol properties over land
882 from inversion of Moderate Resolution Imaging Spectroradiometer spectral

883 reflectance, J Geophys Res-Atmos, 112, Artn D13211Doi
884 10.1029/2006jd007811, 2007b.
885 Levy, R. C., Remer, L. A., Kleidman, R. G., Mattoo, S., Ichoku, C., Kahn, R., and
886 Eck, T. F.: Global evaluation of the collection 5 MODIS dark-target aerosol
887 products over land, Atmos Chem Phys, 10, 10399-10420, DOI
888 10.5194/acp-10-10399-2010, 2010.
889 Levy, R. C., Mattoo, S., Munchak, L. A., Remer, L. A., Sayer, A. M., Patadia, F., and
890 Hsu, N. C.: The Collection 6 MODIS aerosol products over land and ocean,
891 Atmos Meas Tech, 6, 2989-3034, 10.5194/amt-6-2989-2013, 2013.
892 Lyapustin, A., Smirnov, A., Holben, B., Chin, M., Streets, D. G., Lu, Z., Kahn, R.,
893 Slutsker, I., Laszlo, I., Kondragunta, S., Tanre, D., Dubovik, O., Goloub, P.,
894 Chen, H. B., Sinyuk, A., Wang, Y., and Korkin, S.: Reduction of aerosol
895 absorption in Beijing since 2007 from MODIS and AERONET, Geophys
896 Res Lett, 38, Artn L10803 Doi 10.1029/2011gl047306, 2011a.
897 Lyapustin, A., Wang, Y., Laszlo, I., Kahn, R., Korkin, S., Remer, L., Levy, R., and
898 Reid, J. S.: Multiangle implementation of atmospheric correction (MAIAC):
899 2. Aerosol algorithm, J Geophys Res-Atmos, 116, Artn D03211Doi
900 10.1029/2010jd014986, 2011b.
901 Nakajima, T., Yoon, S. C., Ramanathan, V., Shi, G. Y., Takemura, T., Higurashi, A.,
902 Takamura, T., Aoki, K., Sohn, B. J., Kim, S. W., Tsuruta, H., Sugimoto, N.,
903 Shimizu, A., Tanimoto, H., Sawa, Y., Lin, N. H., Lee, C. T., Goto, D., and
904 Schutgens, N.: Overview of the Atmospheric Brown Cloud East Asian
905 Regional Experiment 2005 and a study of the aerosol direct radiative
906 forcing in east Asia, J Geophys Res-Atmos, 112, Artn D24s91

907 Park, M. E., Song, C. H., Park, R. S., Lee, J., Kim, J., Lee, S., Woo, J. H., Carmichael,
908 G. R., Eck, T. F., Holben, B. N., Lee, S. S., Song, C. K., and Hong, Y. D.:
909 New approach to monitor transboundary particulate pollution over
910 Northeast Asia, Atmos Chem Phys, 14, 659-674, 10.5194/acp-14-659-2014,
911 2014.
912 Pope, C. A., and Dockery, D. W.: Health effects of fine particulate air pollution: Lines
913 that connect, J Air Waste Manage, 56, 709-742, 2006.
914 Remer, L. A., Kaufman, Y. J., Tanre, D., Mattoo, S., Chu, D. A., Martins, J. V., Li, R.
915 R., Ichoku, C., Levy, R. C., Kleidman, R. G., Eck, T. F., Vermote, E., and
916 Holben, B. N.: The MODIS aerosol algorithm, products, and validation, J
917 Atmos Sci, 62, 947-973, Doi 10.1175/Jas3385.1, 2005.
918 Saide, P. E., Kim, J., Song, C. H., Choi, M., Cheng, Y. F., and Carmichael, G. R.:
919 Assimilation of next generation geostationary aerosol optical depth
920 retrievals to improve air quality simulations, Geophys Res Lett, 41, 9188-
921 9196, 10.1002/2014gl062089, 2014
922 Sayer, A. M., Hsu, N. C., Bettenhausen, C., Jeong, M. J., Holben, B. N., and Zhang, J.:
923 Global and regional evaluation of over-land spectral aerosol optical depth
924 retrievals from SeaWiFS, Atmos Meas Tech, 5, 1761-1778, 10.5194/amt-5-
925 1761-2012, 2012.
926 Sayer, A. M., Hsu, N. C., Eck, T. F., Smirnov, A., and Holben, B. N.: AERONET-
927 based models of smoke-dominated aerosol near source regions and
928 transported over oceans, and implications for satellite retrievals of aerosol
929 optical depth, Atmos Chem Phys, 14, 11493-11523, 10.5194/acp-14-11493-
930 2014, 2014.

931 Smirnov, A., Holben, B. N., Eck, T. F., Dubovik, O., and Slutsker, I.: Cloud-
932 screening and quality control algorithms for the AERONET database,
933 Remote Sens Environ, 73, 337-349, Doi 10.1016/S0034-4257(00)00109-7,
934 2000.
935 Stocker, T. F., Qin, D., Plattner, G.-K., Tignor, M., Allen, S. K., Boschung, J., Nauels,
936 A., Xia, Y., Bex, V., and Midgley, P. M.: Climate change 2013: The
937 physical science basis, Intergovernmental Panel on Climate Change,
938 Working Group I Contribution to the IPCC Fifth Assessment Report
939 (AR5)(Cambridge Univ Press, New York), 2013.
940 Taylor, K. E.: Summarizing multiple aspects of model performance in a single
941 diagram., J Geophys Res-Atmos, 106, 7183-7192, Doi
942 10.1029/2000jd900719, 2001.
943 Torres, O., Tanskanen, A., Veihelmann, B., Ahn, C., Braak, R., Bhartia, P. K.,
944 Veefkind, P., and Levelt, P.: Aerosols and surface UV products from ozone
945 monitoring instrument observations: An overview, J Geophys Res-Atmos,
946 112, Artn D24s47Doi 10.1029/2007jd008809, 2007.
947 Urm, Y. D., and Sohn, B. J.: Estimation of aerosol optical thickness over East Asia
948 using GMS-5 visible channel measurements, J. of Atmosphere, 15, 203-211,
949 2005.Vermote, E. F., Tanre, D., Deuze, J. L., Herman, M., and Morcrette, J.
950 J.: Second simulation of the satellite signal in the solar spectrum, 6S: An
951 overview, IEEE T Geosci Remote, 35, 675-686, Doi 10.1109/36.581987,
952 1997.
953 von Hoyningen-Huene, W., Yoon, J., Vountas, M., Istomina, L. G., Rohen, G., Dinter,
954 T., Kokhanovsky, A. A., and Burrows, J. P.: Retrieval of spectral aerosol

optical thickness over land using ocean color sensors MERIS and SeaWiFS, Atmos Meas Tech, 4, 151-171, DOI 10.5194/amt-4-151-2011, 2011.

Wang, J., Christopher, S. A., Brechtel, F., Kim, J., Schmid, B., Redemann, J., Russell, P. B., Quinn, P., and Holben, B. N.: Geostationary satellite retrievals of aerosol optical thickness during ACE-Asia, J Geophys Res-Atmos, 108, Artn 8657Doi 10.1029/2003jd003580, 2003.

Waquet, F., Cairns, B., Knobelspiesse, K., Chowdhary, J., Travis, L. D., Schmid, B., and Mishchenko, M. I.: Polarimetric remote sensing of aerosols over land, J Geophys Res-Atmos, 114, Artn D0120610.1029/2008jd010619, 2009.

Wong, M. S., Lee, K. H., Nichol, J. E., and Li, Z. Q.: Retrieval of aerosol optical thickness using MODIS 500 x 500 m(2), a study in Hong Kong and the pearl river delta region, IEEE T Geosci Remote, 48, 3318-3327, Doi 10.1109/Tgrs.2010.2045124, 2010.

Yang, P., Feng, Q., Hong, G., Kattawar, G. W., Wiscombe, W. J., Mishchenko, M. I., Dubovik, O., Laszlo, I., and Sokolik, I. N.: Modeling of the scattering and radiative properties of nonspherical dust-like aerosols, J Aerosol Sci, 38, 995-1014, DOI 10.1016/j.jacrosci.2007.07.001, 2007.

Yoon, J.-M.: Effects of atmospheric and surface properties on the retrieval of AOD from geostationary satellite, PH.D. thesis, Department of Atmospheric Scinces, Yonsei Univ, Seoul, Republic of Korea, 2006.

Yoon, J. M., Kim, J., Lee, J. H., Cho, H. K., Sohn, B. J., and Ahn, M. A.: Retrieved of aerosol optical depth over East Asia from a geostationary satellite, MTSAT-1R, Asia-Pacific J. Atmos. Sci., 43, 133-142, 2007.

Yoon, J., Burrows, J. P., Vountas, M., von Hoyningen-Huene, W., Chang, D. Y., Richter, A., and Hilboll, A.: Changes in atmospheric aerosol loading

retrieved from space-based measurements during the past decade, Atmos Chem Phys, 14, 6881-6902, DOI 10.5194/acp-14-6881-2014, 2014.

Zhang, H., Lyapustin, A., Wang, Y., Kondragunta, S., Laszlo, I., Ciren, P., and Hoff, R. M.: A multi-angle aerosol optical depth retrieval algorithm for geostationary satellite data over the United States, Atmos Chem Phys, 11, 11977-11991, DOI 10.5194/acp-11-11977-2011, 2011.

Zhang, J. L., Christopher, S. A., and Holben, B. N.: Intercomparison of smoke aerosol optical thickness derived from GOES 8 imager and ground-based sun photometers, J Geophys Res-Atmos, 106, 7387-7397, Doi 10.1029/2000jd900540, 2001.

991 **List of Tables**

992

993 Table 1. Summary of AERONET sites used in this study. Columns “Period” represent
994 the retrieval period of the daily inversion product (level 2.0), and the
995 longitude (long., °E) and latitude (lat., °N) show the location for each site.
996 The number in front of the site name lists the sites operated for the
997 DRAGON-Asia campaign, where “D” is the initial of the campaign. The
998 numbers are linked to Table 4, Table 5, and Figure 9. The color and type of
999 character categorizes the inversion dataset into the "original", "new", and
1000 "excepted" groups. While the "original" group is compiled from the
1001 inversion datasets obtained before 2011 at sites in grey cell, the "new"
1002 group consists of the total dataset excluding the "excepted" group shown in
1003 bold and italic type.
1004 Table 2. Integrated AOPs at each AOD bin (550 nm) from AERONET inversion data.
1005 Each of the AOD bins ranges between 0.0-0.3, 0.3-0.6, 0.6-1.0, 1.0-1.4,
1006 1.4-1.8, and 1.8-3.0, respectively, and the median value is shown in the
1007 Table. The values in (a) (upper panel) were obtained from the original
1008 inversion data group, and those in the middle and lower panels (b and c)
1009 were estimated from temporally and temporal-spatially extended datasets,
1010 respectively.
1011 Table 3. Summary statistics of the comparison between the MI AOD [550 nm]
1012 retrieved with the original LUT and AERONET AOD [550 nm]. The site
1013 numbers correspond to the number listed in Table 1 and Figure 10(a). The
1014 sites mentioned in section 4.2 are represented by grey shade.

1015 Table 4. Summary statistics of the comparison between the MI AOD [550 nm]
1016 retrieved with the updated LUT and AERONET AOD [550 nm]. The site
1017 numbers correspond to the number listed in Table 1 and Figure 10(b). The
1018 sites mentioned in section 4.2 are represented by grey shade.
1019
1020

1021 **List of Figures**

1022

in Table 2. The size distributions are averaged for each AOD interval, and the color of the curve indicates the mean AOD value.

Figure 6. Dependence of the AOD retrieval error on error in assumed SSA for four different AOD cases. The SSA error represents the percentage difference between SSAs used to the simulation and the retrieval, and the AOD error indicates the difference between the retrieved AOD and a reference value. Surface reflectance is assumed to be 0.05, and scattering angles ranging from 135.73° to 173.23° are applied. The error bars indicate the standard deviation of AOD error obtained from the geometric variation, and the numbers in parentheses are the SSA error without the inversion error.

Figure 7. Uncertainties in retrieval of AOD and surface reflectance; (a), (b) AOD error depending on scattering angle for two cases of AOD [0.15, 1.20] and two cases surface reflectance [0.05, 0.10]; (c) error in surface reflectance according to BAOD assumption error for three conditions of BAOD [0.05, 0.10, 0.15]; and (d) sensitivity of AOD error to error in surface reflectance and elevation for each assumed condition of AOD.

Figure 8. RGB images obtained from GOCI measurement and examples of retrieved AOD from MI measurement on April 27, 2012. Two panels at left bottom side are the MODIS AOD product obtained from TERRA (MOD04) and AQUA (MYD04) measurements. The AOD ranges between 0 and 2 in those panels.

Figure 9. Evaluation of the AOD retrieved from MI measurements during DRAGON-Asia. The x-axis and y-axis indicate the values of AOD at 550 nm obtained from AERONET and MI measurements, respectively, and the color of the symbols shows the data counts for each AOD bin. The y-axis on the left [(a)

and (c)] and right side [(b) and (d)] represents the AOD retrieved using the original and new LUT, respectively. The plots on the top [(a) and (b)] contain the data measured from all campaign sites, whereas those on the bottom [(c) and (d)] contain only the values from the sites excluded in the AOP analysis. The linear regression line with a Pearson coefficient (r) and root mean square error (RMSE) were included for each plot.

Figure 10. Taylor diagrams comparing the retrieved AODs and the values obtained from AERONET sun-photometer measurements during the DRAGON-2012 campaign. (a): Comparison of results from the original AOD, (b): comparison of results from the new AOD. The numbers above each symbol indicate the number of the DRAGON-Asia site, as listed in Table 1.

Figure 11. Temporal variations of AODs during the DRAGON-Asia. The red box and black circle represent the values retrieved from MI and AERONET measurement, respectively, and each panel shows the time series for different AERONET sites; (a) Anmyeon, (b) Kunsan_NU, (c) Kohriyama, (d) Nishiharima.

Table 1. Summary of AERONET sites used in this study. Columns “Period” represent the retrieval period of the daily inversion product (level 2.0), and the longitude (long., °E) and latitude (lat., °N) show the location for each site. The number in front of the site name lists the sites operated for the DRAGON-Asia campaign, where “D” is the initial of the campaign. The numbers are linked to Table 4, Table 5, and Figure 9. The color and type of character categorizes the inversion dataset into the "original", "new", and "excepted" groups. While the "original" group is compiled from the inversion datasets obtained before 2011 at sites in grey cell, the "new" group consists of the total dataset excluding the "excepted" group shown in bold and italic type.

1097

Site	Long.	Lat.	Period	Site	Long.	Lat.	Period
(1) Baengnyeong	124.63	37.97	2010-2013	*(36) Osaka*	*135.59*	*34.65*	*2001-2013*
(2) Chiba_University	140.1	35.63	2011-2012	(37) Seoul_SNU	126.95	37.46	2000-2013
(3) D_Anmyeon	126.33	36.54	DRAGON2012*	*(38) Shirahama*	*135.36*	*33.69*	*2000-2013*
(4) D_Bokjeong	127.13	37.46	DRAGON2012	(39) Yonsei_University	126.93	37.56	2011-2013
(5) D_Fukue	**128.68**	**32.75**	**DRAGON2012**	*Anmyon*	*126.33*	*36.54*	*1999-2007*
(6) D_Fukue_2	**128.82**	**32.67**	**DRAGON2012**	*Bac_Giang*	*106.23*	*21.29*	*2003-2009*
(7) D_Fukuoka	130.48	33.52	DRAGON2012	Bach_Long_Vy	107.73	20.13	2010-2011
(8) D_GangneungWNU	**128.87**	**37.77**	**DRAGON2012**	*Beijing*	*116.38*	*39.98*	*2001-2013*
(9) D_Guwol	126.72	37.45	DRAGON2012	*Chen-Kung_Univ*	*120.22*	*23*	*2002-2012*
(10) D_Hankuk_UFS	**127.27**	**37.34**	**DRAGON2012**	*Dongsha_Island*	*116.73*	*20.7*	*2004-2013*
(11) D_Kobe	135.29	34.72	DRAGON2012	*EPA-NCU*	*121.19*	*24.97*	*2006-2013*
(12) D_Kohriyama	140.38	37.36	DRAGON2012	Hangzhou-ZFU	119.73	30.26	2007-2007
(13) D_Kongju_NU	127.14	36.47	DRAGON2012	Hefei	117.16	31.91	2005-2008
(14) D_Konkuk_Univ	127.08	37.54	DRAGON2012	*Hong_Kong_Hok_Tsui*	*14.26*	*22.21*	*2007-2010*
(15) D_Korea_Univ	**127.03**	**37.58**	**DRAGON2012**	*Hong_Kong_PolyU*	*114.18*	*22.3*	*2005-2013*
(16) D_Kunsan_NU	126.68	35.94	DRAGON2012	*Inner_Mongolia*	*115.95*	*42.68*	*2001-2001*
(17) D_Kyoto	135.78	35.03	DRAGON2012	Jingtai	104.1	37.33	2008-2008
(18) D_Kyungil_Univ	**128.82**	**36.07**	**DRAGON2012**	Lanzhou_City	103.85	36.05	2009-2010
(19) D_Matsue	**133.01**	**35.48**	**DRAGON2012**	Liangning	122.7	41.51	2005-2005
(20) D_Mokpo_NU	**126.44**	**34.91**	**DRAGON2012**	Luang_Namtha	101.42	20.93	2012-2014
(21) D_Mt_Ikoma	**135.68**	**34.68**	**DRAGON2012**	*Lulin*	*120.87*	*23.47*	*2007-2014*
(22) D_Mt_Rokko	**135.23**	**34.76**	**DRAGON2012**	Minqin	102.96	38.61	2010-2010
(23) D_NIER	126.64	37.57	DRAGON2012	NGHIA_DO	105.8	21.05	2010-2013
(24) D_Nara	135.83	34.69	DRAGON2012	PKU_PEK	116.18	39.59	2006-2008
(25) D_Nishiharima	134.34	35.03	DRAGON2012	SACOL	104.14	35.95	2006-2012
(26) D_Osaka-North	135.51	34.77	DRAGON2012	Shouxian	116.78	32.56	2008-2008
(27) D_Osaka-South	135.5	34.54	DRAGON2012	*Taichung*	*120.49*	*24.11*	*2005-2005*
(28) D_Pusan_NU	129.08	35.24	DRAGON2012	Taihu	120.22	31.42	2005-2012
(29) D_Sanggye	127.07	37.66	DRAGON2012	*Taipei_CWB*	*121.5*	*25.03*	*2002-2013*
(30) D_Sinjeong	**126.86**	**37.52**	**DRAGON2012**	*Ussuriysk*	*132.16*	*43.7*	*2004-2013*
(31) D_Soha	126.89	37.45	DRAGON2012	XiangHe	116.96	39.75	2001-2012
(32) D_Tsukuba	140.12	36.05	DRAGON2012	Xinglong	117.58	40.4	2006-2012
(33) Gosan_SNU	*126.16*	*33.29*	*2001-2013*	Yufa_PEK	116.18	39.31	2006-2006
(34) Gwangju_GIST	*126.84*	*35.23*	*2004-2012*	Zhangye	100.28	39.08	2008-2008
(35) Noto	**137.14**	**37.33**	**2001-2013**				

1098 *DRAGON2012 : Period of DRADON-Asia 2012 campaign [March –May, 2012]

1099

Table 2. Integrated AOPs for each AOD bin (550 nm) from AERONET inversion data. Each of the AOD bins ranges between 0.0-0.3, 0.3-0.6, 0.6-1.0, 1.0-1.4, 1.4-1.8, and 1.8-3.0, respectively, and the median value is shown in the Table. The values in (a) (upper panel) were obtained from the original inversion data group, and those in the middle and lower panels (b and c) were estimated from temporally and temporal-spatially extended datasets, respectively.

(a) Original Aerosol Model	AOD					
	0.15	0.45	0.8	1.2	1.6	>2.6
SSA at 675 nm	0.911	0.921	0.928	0.932	0.939	0.945
Refractive index [Real] at 675 nm(STD)	1.47(0.06)	1.47(0.05)	1.47(0.05)	1.49(0.05)	1.53(0.05)	1.52(0.06)
Refractive index [Im.] at 675 nm(STD)	0.0085 (0.0046)	0.0075 (0.0050)	0.0077 (0.0049)	0.0075 (0.0044)	0.0060 (0.0041)	0.0050 (0.0032)
Effective Radius-F (μm)	0.14	0.15	0.18	0.19	0.18	0.20
Effective Radius-C (μm)	1.76	1.90	2.08	2.16	2.01	2.03
Standard deviation-F	0.45	0.47	0.51	0.54	0.55	0.56
Standard deviation-C	0.69	0.64	0.62	0.58	0.54	0.52
Number of data	55	528	270	87	26	21
(b) Updated Aerosol Model (temporally extended)	**AOD**					
	0.15	0.45	0.8	1.2	1.6	>2.6
SSA at 675 nm	0.910	0.923	0.932	0.935	0.940	0.949
Refractive index [Real] at 675 nm(STD)	1.48(0.06)	1.47(0.05)	1.48(0.05)	1.49(0.05)	1.52(0.05)	1.51(0.05)
Refractive index [Im.] at 675 nm(STD)	0.0083 (0.0049)	0.0072 (0.0086)	0.0071 (0.0047)	0.0070 (0.0044)	0.0059 (0.0036)	0.0048 (0.0031)
Effective Radius-F (μm)	0.14	0.15	0.17	0.18	0.18	0.20
Effective Radius-C (μm)	1.84	1.94	2.09	2.16	2.02	2.01
Standard deviation-F	0.45	0.47	0.51	0.54	0.53	0.56
Standard deviation-C	0.69	0.64	0.61	0.58	0.55	0.53
Number of data	75	677	370	112	37	31
(c) Updated Aerosol Model (temporal-spatially extended)	**AOD**					
	0.15	0.45	0.8	1.2	1.6	>2.6
SSA at 675 nm	0.916	0.927	0.935	0.940	0.944	0.951
Refractive index [Real] at 675 nm(STD)	1.48(0.06)	1.48(0.05)	1.48(0.05)	1.50(0.05)	1.51(0.05)	1.51(0.05)
Refractive index [Im.] at 675 nm(STD)	0.0073 (0.0043)	0.0065 (0.0072)	0.0061 (0.0041)	0.0060 (0.0040)	0.0054 (0.0039)	0.0046 (0.0037)
Effective Radius-F (μm)	0.14	0.15	0.16	0.17	0.17	0.20
Effective Radius-C (μm)	1.87	1.95	2.07	2.11	2.05	1.98
Standard deviation-F	0.46	0.48	0.51	0.55	0.57	0.56
Standard deviation-C	0.69	0.65	0.61	0.58	0.55	0.54
Number of data	219	1431	767	235	74	51

Table 3. Summary statistics of the comparison between the MI AOD [550 nm] retrieved with the

original LUT and AERONET AOD [550 nm]. The site numbers correspond to the number listed in Table 1 and Figure 9(a). The sites mentioned in section 4.2 are represented by grey shade.

Site No.	datan	MI AOD mean(STD)	DRAGON AOD mean(STD)	AOD Diff.	R	slope	y-offset	RMSE
1	400	0.42(0.34)	0.43(0.25)	-0.010	0.942	1.278	-0.13	0.115
2	76	0.43(0.21)	0.36(0.16)	0.071	0.814	1.054	0.051	0.122
3	**273**	**0.51(0.39)**	**0.55(0.31)**	**-0.033**	**0.949**	**1.190**	**-0.138**	**0.121**
4	**341**	**0.63(0.34)**	**0.66(0.26)**	**-0.023**	**0.829**	**1.101**	**-0.089**	**0.192**
5	408	0.52(0.37)	0.70(0.36)	-0.172	0.891	0.915	-0.112	0.167
6	4	0.61(0.17)	0.68(0.02)	-0.067	0.927	7.337	-4.359	0.056
7	109	0.36(0.24)	0.41(0.17)	-0.049	0.859	1.198	-0.130	0.122
8	182	0.46(0.22)	0.50(0.18)	-0.044	0.771	0.955	-0.021	0.141
9	458	0.56(0.35)	0.55(0.26)	0.004	0.871	1.164	-0.087	0.169
10	275	0.57(0.32)	0.59(0.26)	-0.019	0.875	1.077	-0.065	0.156
11	108	0.45(0.27)	0.51(0.22)	-0.062	0.782	0.966	-0.045	0.165
12	**23**	**0.58(0.29)**	**0.45(0.16)**	**0.138**	**0.849**	**1.581**	**-0.122**	**0.152**
13	232	0.67(0.47)	0.68(0.37)	-0.012	0.914	1.154	-0.117	0.190
14	355	0.58(0.35)	0.64(0.27)	-0.065	0.862	1.118	-0.140	0.179
15	430	0.60(0.35)	0.66(0.27)	-0.063	0.846	1.102	-0.130	0.189
16	227	0.70(0.50)	0.67(0.44)	0.031	0.952	1.104	-0.039	0.153
17	47	0.49(0.31)	0.54(0.21)	-0.047	0.778	1.111	-0.107	0.190
18	272	0.43(0.27)	0.49(0.21)	-0.066	0.812	1.051	-0.091	0.159
19	**56**	**0.60(0.28)**	**0.64(0.16)**	**-0.035**	**0.776**	**1.345**	**-0.254**	**0.173**
20	254	0.66(0.32)	0.60(0.26)	0.058	0.890	1.090	0.003	0.147
21	71	0.41(0.21)	0.42(0.18)	-0.009	0.834	0.987	-0.003	0.117
22	112	0.44(0.21)	0.41(0.14)	0.035	0.775	1.199	-0.047	0.132
23	206	0.66(0.37)	0.58(0.25)	0.081	0.892	1.336	-0.114	0.167
24	82	0.37(0.26)	0.45(0.20)	-0.086	0.907	1.185	-0.170	0.107
25	**46**	**0.30(0.21)**	**0.42(0.16)**	**-0.120**	**0.656**	**0.862**	**-0.062**	**0.159**
26	69	0.40(0.23)	0.48(0.22)	-0.087	0.858	0.925	-0.050	0.119
27	138	0.49(0.32)	0.51(0.21)	-0.029	0.778	1.162	-0.112	0.197
28	317	0.48(0.29)	0.55(0.25)	-0.063	0.871	1.006	-0.067	0.143
29	336	0.62(0.38)	0.67(0.29)	-0.054	0.835	1.080	-0.108	0.206
30	246	0.62(0.40)	0.63(0.27)	-0.009	0.868	1.259	-0.171	0.197
31	437	0.60(0.35)	0.61(0.26)	-0.015	0.821	1.104	-0.078	0.200
32	135	0.50(0.27)	0.35(0.17)	0.144	0.703	1.152	0.090	0.194
33	458	0.56(0.39)	0.62(0.33)	-0.051	0.942	1.099	-0.112	0.130
34	290	0.63(0.38)	0.63(0.27)	0.004	0.913	1.274	-0.169	0.156
35	93	0.41(0.24)	0.43(0.17)	-0.017	0.935	1.303	-0.147	0.086
36	115	0.43(0.29)	0.51(0.20)	-0.087	0.787	1.140	-0.159	0.178
37	260	0.61(0.35)	0.61(0.27)	-0.001	0.835	1.097	-0.060	0.194
38	92	0.32(0.20)	0.38(0.14)	-0.055	0.804	1.136	-0.107	0.121
39	316	0.64(0.37)	0.65(0.26)	-0.018	0.805	1.140	-0.110	0.219

Table 4. Summary statistics of the comparison between the MI AOD [550 nm] retrieved with the

updated LUT and AERONET AOD [550 nm]. The site numbers correspond to the number listed in Table 1 and Figure 9(a). The sites mentioned in section 4.2 are represented by grey shade.

Site No.	datan	MI AOD mean(STD)	DRAGON AOD mean(STD)	AOD Diff.	R	slope	y-offset	RMSE
1	402	0.39(0.32)	0.43(0.25)	-0.033	0.944	1.205	-0.121	0.107
2	76	0.40(0.19)	0.36(0.16)	0.045	0.812	0.965	0.058	0.112
3	284	0.49(0.39)	0.55(0.32)	-0.058	0.949	1.139	-0.134	0.122
4	340	0.58(0.31)	0.66(0.26)	-0.072	0.803	0.974	-0.055	0.185
5	413	0.50(0.35)	0.69(0.36)	-0.195	0.882	0.856	-0.095	0.164
6	4	0.58(0.16)	0.68(0.02)	-0.097	0.926	6.857	-4.062	0.053
7	108	0.34(0.22)	0.41(0.17)	-0.064	0.853	1.113	-0.110	0.116
8	186	0.44(0.21)	0.50(0.18)	-0.066	0.763	0.894	-0.013	0.136
9	454	0.51(0.32)	0.55(0.26)	-0.038	0.847	1.036	-0.057	0.167
10	276	0.53(0.30)	0.59(0.26)	-0.065	0.854	0.973	-0.049	0.155
11	111	0.41(0.25)	0.50(0.21)	-0.087	0.775	0.896	-0.035	0.155
12	22	0.56(0.28)	0.45(0.16)	0.103	0.854	1.537	-0.141	0.143
13	242	0.62(0.44)	0.68(0.37)	-0.056	0.902	1.073	-0.106	0.190
14	353	0.53(0.33)	0.64(0.27)	-0.111	0.842	1.014	-0.120	0.176
15	431	0.56(0.33)	0.66(0.27)	-0.108	0.830	1.019	-0.120	0.186
16	234	0.64(0.46)	0.66(0.42)	-0.013	0.949	1.040	-0.039	0.147
17	44	0.43(0.24)	0.52(0.21)	-0.088	0.805	0.928	-0.050	0.139
18	276	0.40(0.26)	0.49(0.21)	-0.092	0.787	0.979	-0.081	0.157
19	56	0.59(0.28)	0.64(0.16)	-0.054	0.745	1.290	-0.240	0.183
20	261	0.60(0.29)	0.59(0.26)	0.005	0.880	0.984	0.015	0.138
21	71	0.38(0.20)	0.42(0.18)	-0.036	0.832	0.919	-0.002	0.111
22	111	0.41(0.19)	0.41(0.13)	0.006	0.765	1.087	-0.029	0.123
23	208	0.62(0.35)	0.58(0.26)	0.034	0.885	1.179	-0.070	0.164
24	82	0.34(0.23)	0.45(0.19)	-0.104	0.895	1.098	-0.148	0.104
25	46	0.29(0.20)	0.42(0.16)	-0.134	0.652	0.802	-0.051	0.150
26	70	0.38(0.23)	0.49(0.22)	-0.104	0.835	0.882	-0.047	0.125
27	137	0.46(0.31)	0.52(0.21)	-0.058	0.774	1.112	-0.116	0.194
28	315	0.45(0.26)	0.54(0.25)	-0.097	0.852	0.900	-0.042	0.136
29	338	0.57(0.36)	0.67(0.29)	-0.098	0.816	0.997	-0.096	0.206
30	245	0.57(0.37)	0.63(0.27)	-0.058	0.842	1.129	-0.138	0.197
31	440	0.55(0.33)	0.61(0.27)	-0.060	0.798	0.997	-0.058	0.201
32	**138**	**0.46(0.25)**	**0.35(0.17)**	**0.104**	**0.710**	**1.080**	**0.075**	**0.179**
33	460	0.53(0.37)	0.61(0.33)	-0.080	0.938	1.042	-0.106	0.128
34	294	0.59(0.37)	0.64(0.28)	-0.048	0.917	1.181	-0.163	0.146
35	93	0.40(0.24)	0.43(0.18)	-0.033	0.936	1.227	-0.132	0.082
36	117	0.42(0.31)	0.52(0.20)	-0.104	0.770	1.171	-0.193	0.197
37	261	0.56(0.33)	0.61(0.27)	-0.051	0.803	0.977	-0.036	0.194
38	94	0.30(0.19)	0.37(0.15)	-0.066	0.799	1.037	-0.079	0.113
39	318	0.59(0.35)	0.65(0.26)	-0.066	0.786	1.042	-0.093	0.217

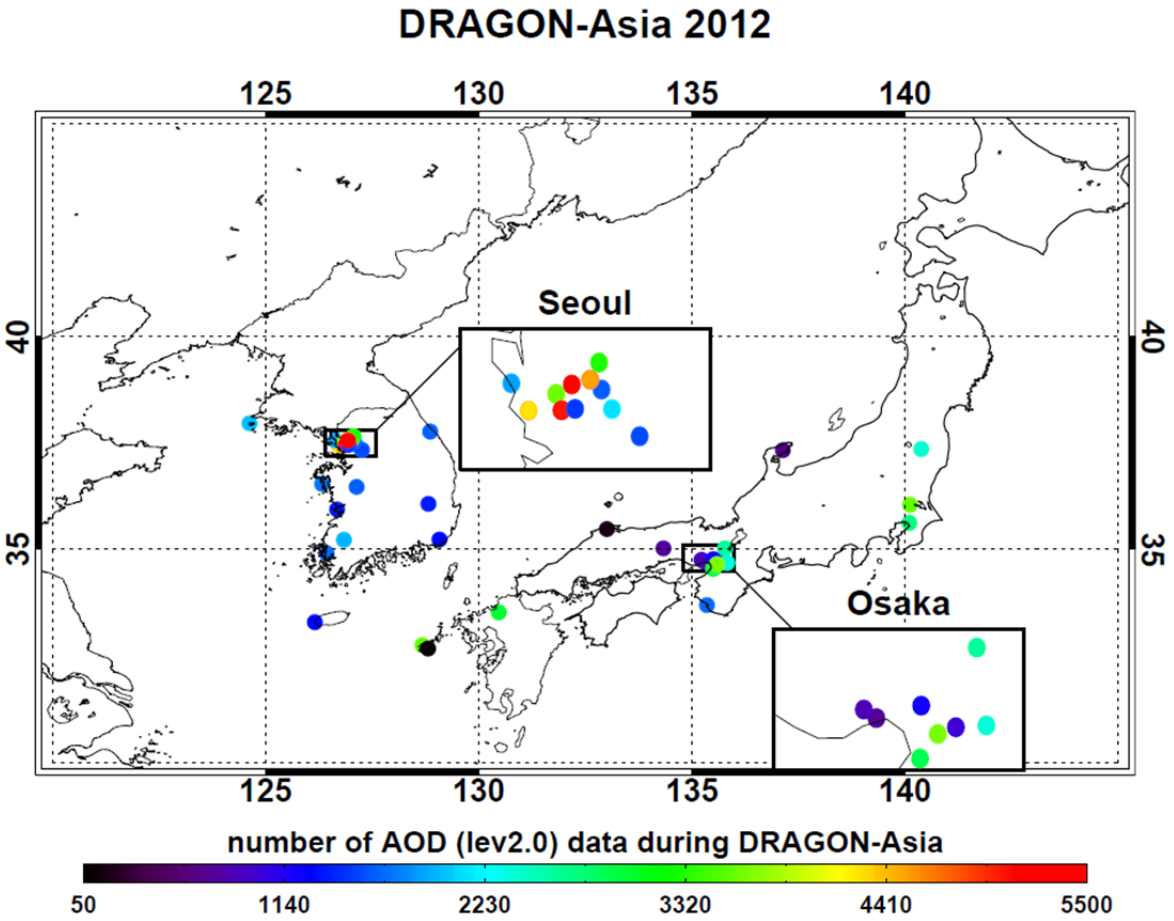

Figure 1. Location and number of data points of the AERONET sun-photometers deployed during DRAGON-NE Asia 2012. The color of each symbol represents the number of AOD [level 2.0] data points measured for the campaign.

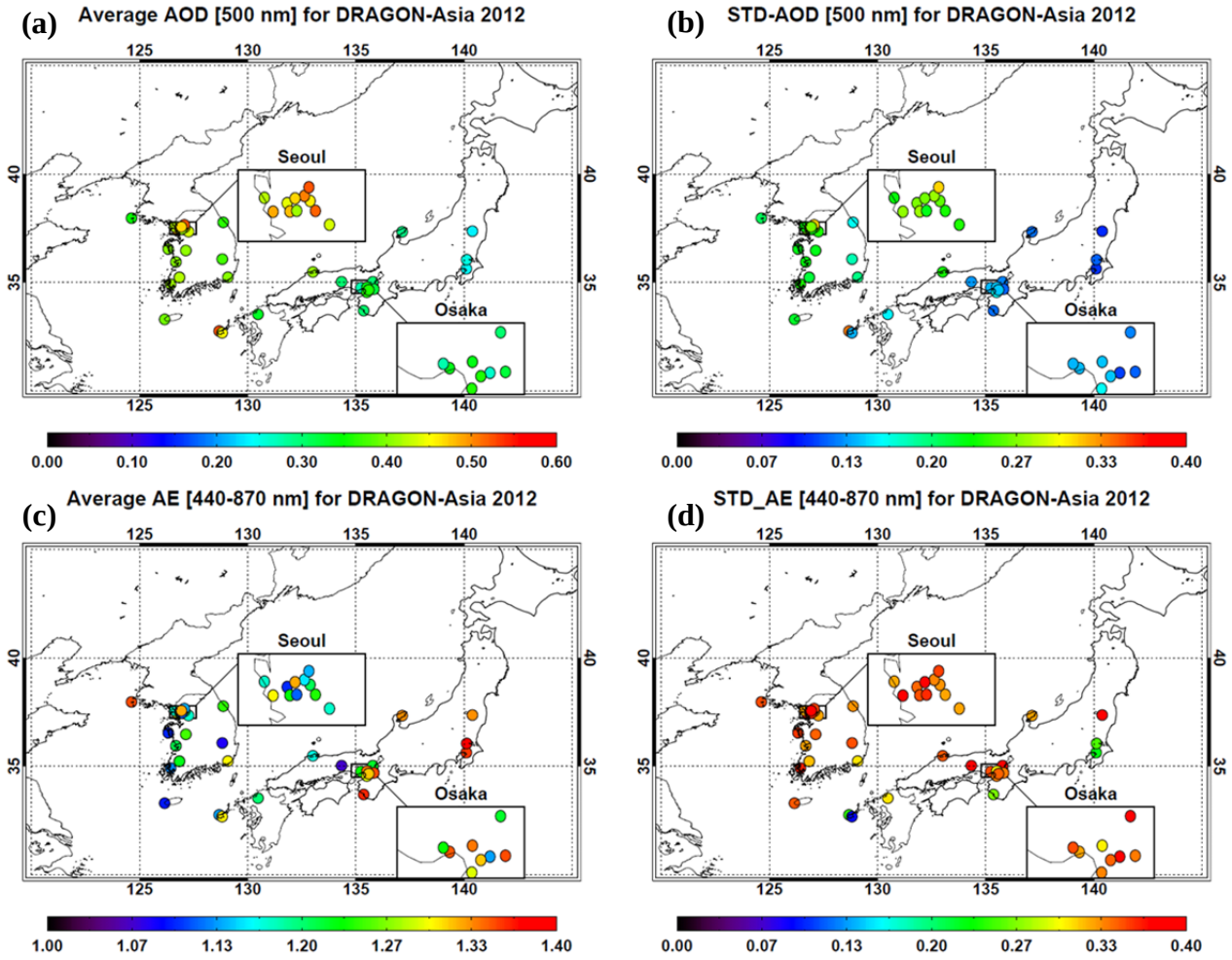

Figure 2. The (a, c) average and (b, d) standard deviation (1σ) of (a, b) AOD at 500 nm and (c, d) Ångström Exponent between 440 nm and 870 nm during DRAGON-NE Asia 2012 campaign for each site

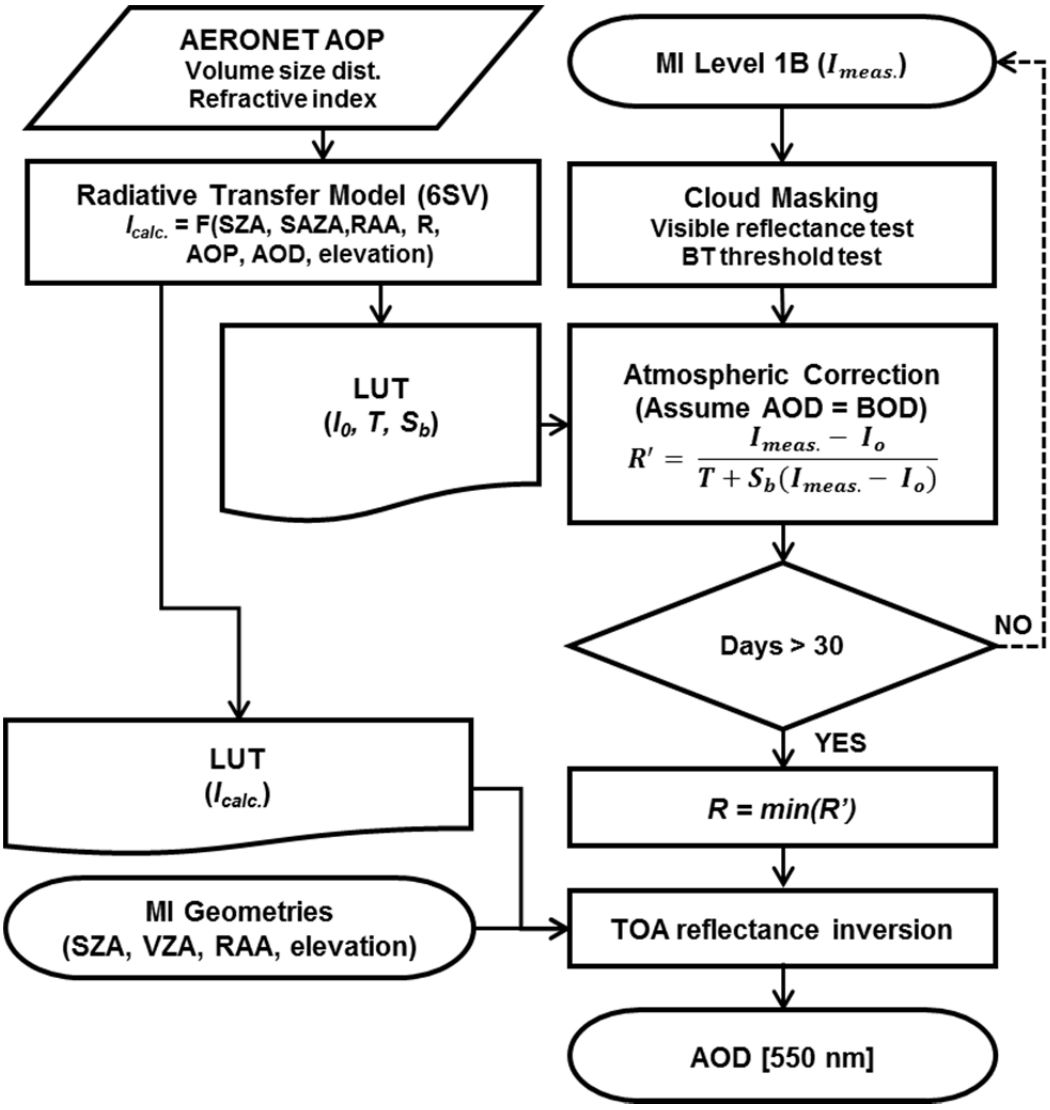

Figure 3. Flowchart of a single channel algorithm for AOD retrieval, adapted from Kim et al. (2014). I_{meas} and I_{calc} represent measured and calculated TOA reflectance, respectively. I_o means atmospheric reflectance including the Rayleigh scattering and aerosol effect, S_b is the hemispheric reflectance, and T is the atmospheric transmittance for the geometry of the sun illumination and satellite viewing. R' shows semi-surface reflectance obtained by correcting the atmospheric effects from the I_{meas}. and the minimum value among the 30-day R' is regarded as the surface reflectance (R).

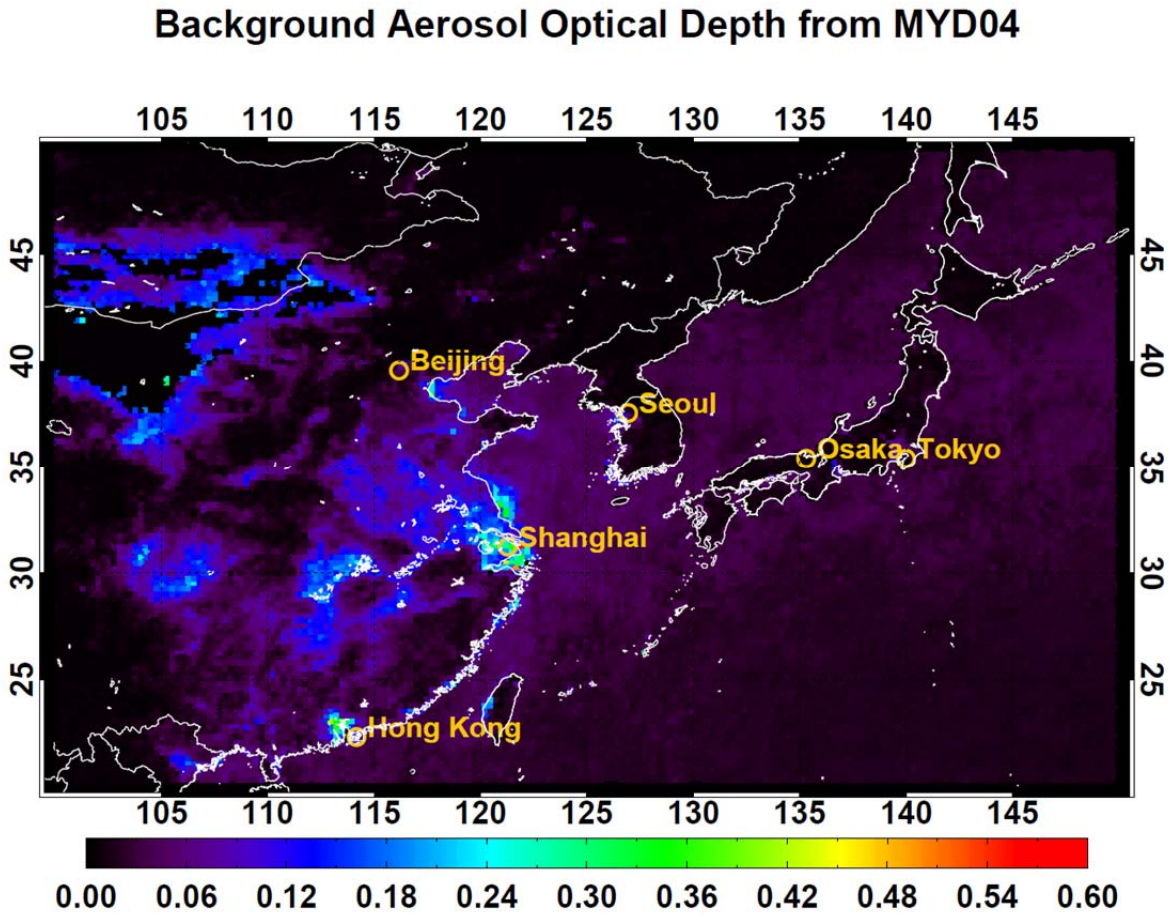

Figure 4. Absolute minimum AOD at 550 nm obtained from MODIS level 2.0 products (MYD04_Lv2.0) from 2006 to 2012 at 0.25° × 0.25° resolution. Yellow circle indicate location of well-known urban area over North East Asia.

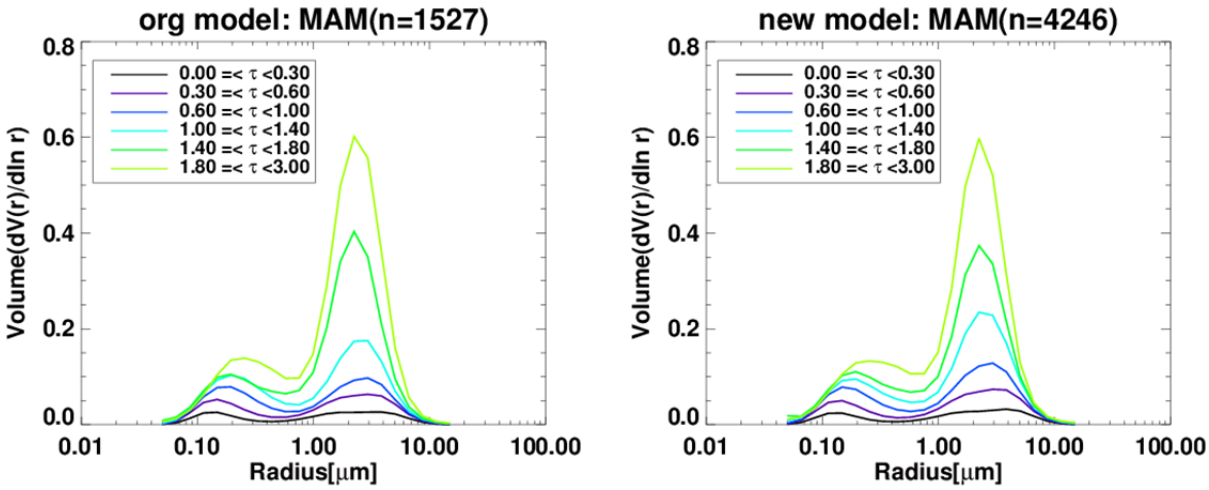

Figure 5. Volume size distribution for each AOD bins, as obtained from the original and new AERONET inversion data listed in Table 1. The effective radius and standard deviation of the find and coarse mode particles are described in Table2. The size distributions are averaged for each AOD interval, and the color of the curve indicates the mean AOD value.

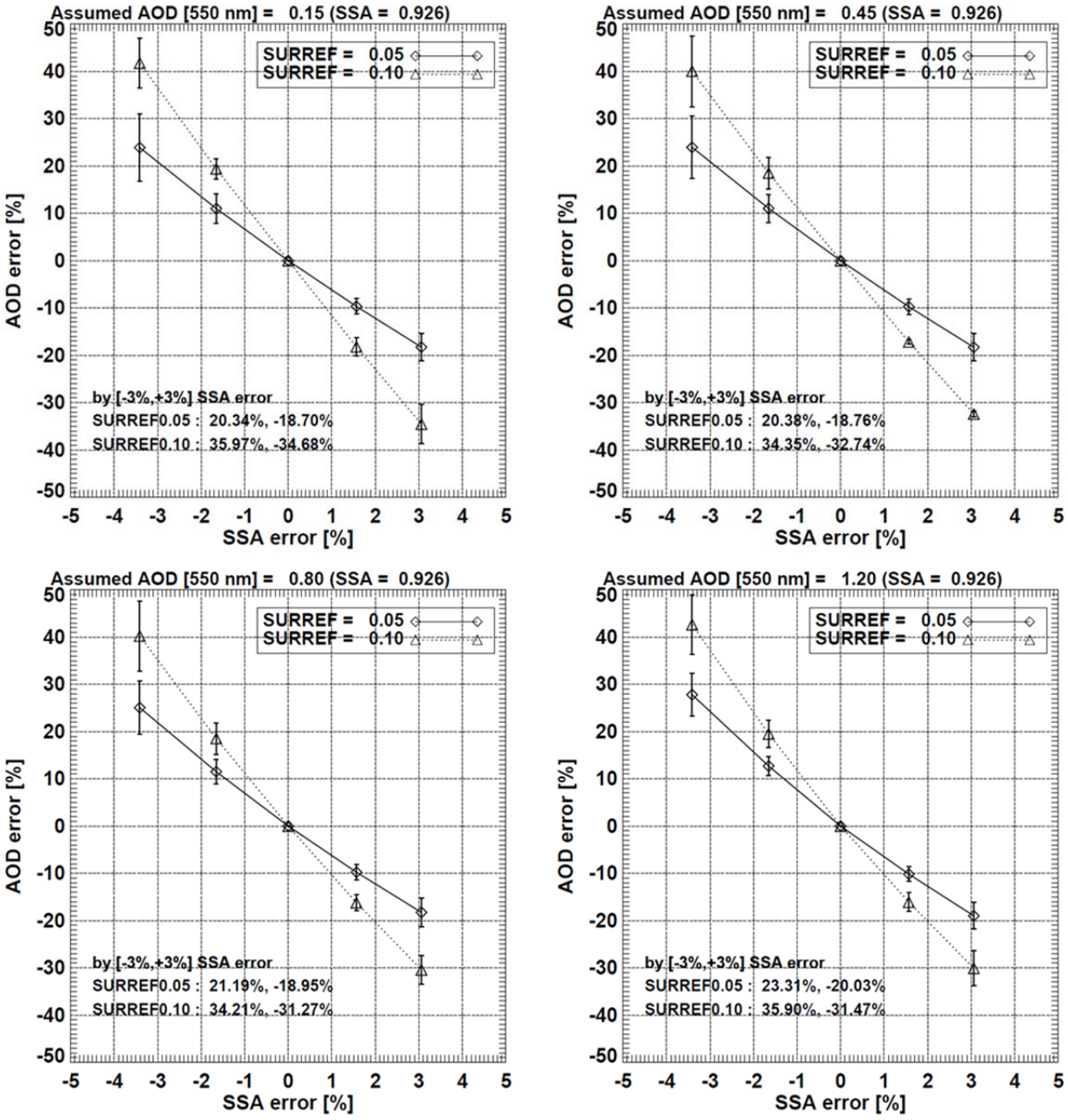

Figure 6. Dependence of the AOD retrieval error on error in assumed SSA for four different AOD cases. The SSA error represents the percentage difference between SSAs used to the simulation and the retrieval, and the AOD error indicates the difference between the retrieved AOD and a reference value. Surface reflectance is assumed to be 0.05, and scattering angles ranging from 135.73° to 173.23° are applied. The error bars indicate the standard deviation of AOD error obtained from the geometric variation, and the numbers in parentheses are the SSA error without the inversion error.

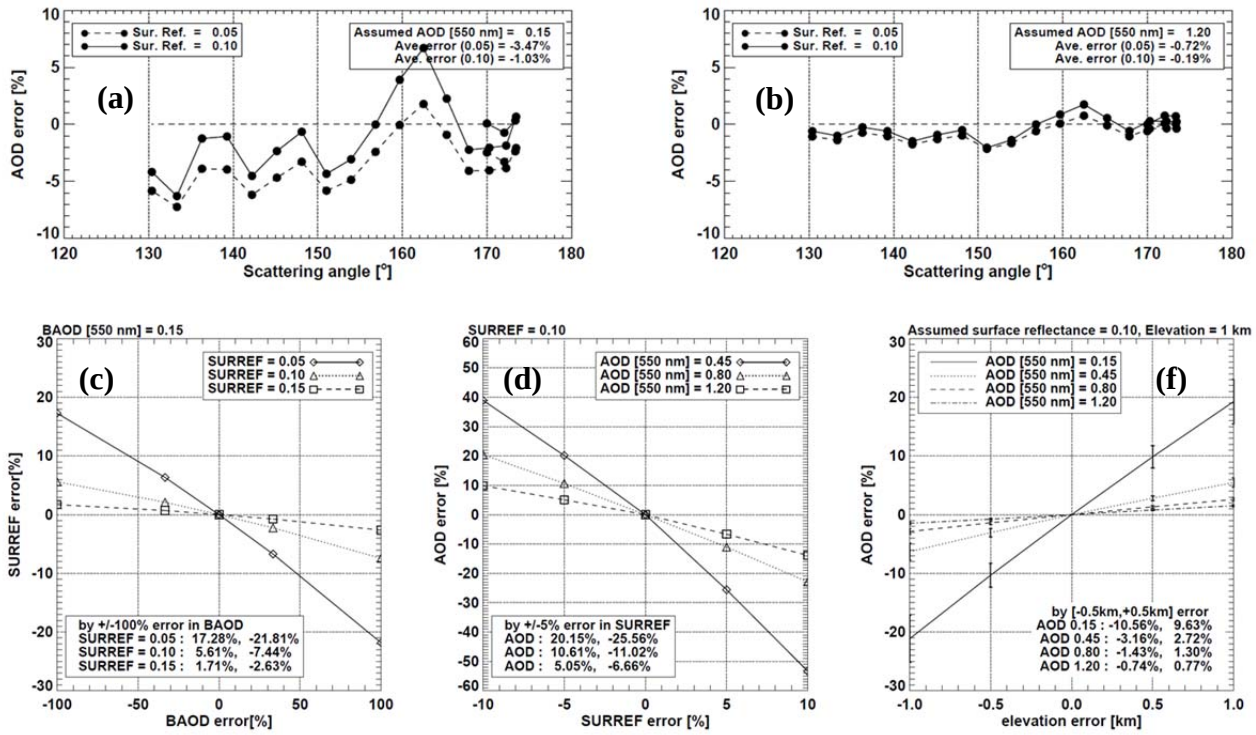

Figure 7. Uncertainties in retrieval of AOD and surface reflectance; (a), (b) AOD error depending on scattering angle for two cases of AOD [0.15, 1.20] and two cases surface reflectance [0.05, 0.10]; (c) error in surface reflectance according to BAOD assumption error for three conditions of BAOD [0.05, 0.10, 0.15]; and (d) sensitivity of AOD error to error in surface reflectance and elevation for each assumed condition of AOD.

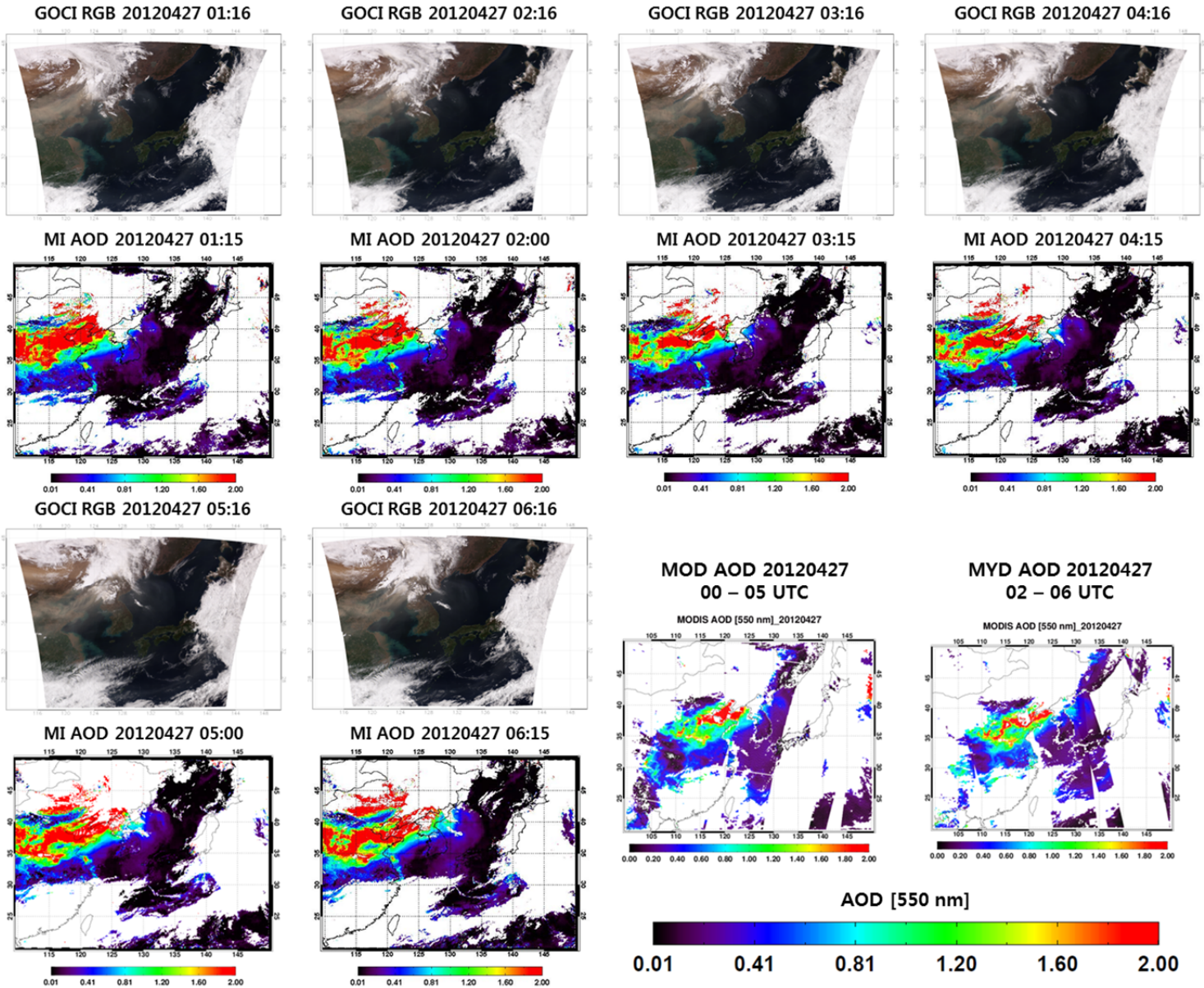
GOCI RGB 20120427 01:16
GOCI RGB 20120427 02:16
GOCI RGB 20120427 03:16
GOCI RGB 20120427 04:16
MI AOD 20120427 01:15
MI AOD 20120427 02:00
MI AOD 20120427 03:15
MI AOD 20120427 04:15
GOCI RGB 20120427 05:16
GOCI RGB 20120427 06:16
MI AOD 20120427 05:00
MI AOD 20120427 06:15
MOD AOD 20120427
00 – 05 UTC
MODIS AOD [550 nm]_20120427
MYD AOD 20120427
02 – 06 UTC
MODIS AOD [550 nm]_20120427
AOD [550 nm]
0.01 0.41 0.81 1.20 1.60 2.00

1164 Figure 8. RGB images obtained from GOCI measurement and examples of retrieved AOD from MI measurement on April 27, 2012. Two panels
1165 at left bottom side are the MODIS AOD product obtained from TERRA (MOD04) and AQUA (MYD04) measurements. The AOD ranges
1166 between 0 and 2 in those panels.

1167

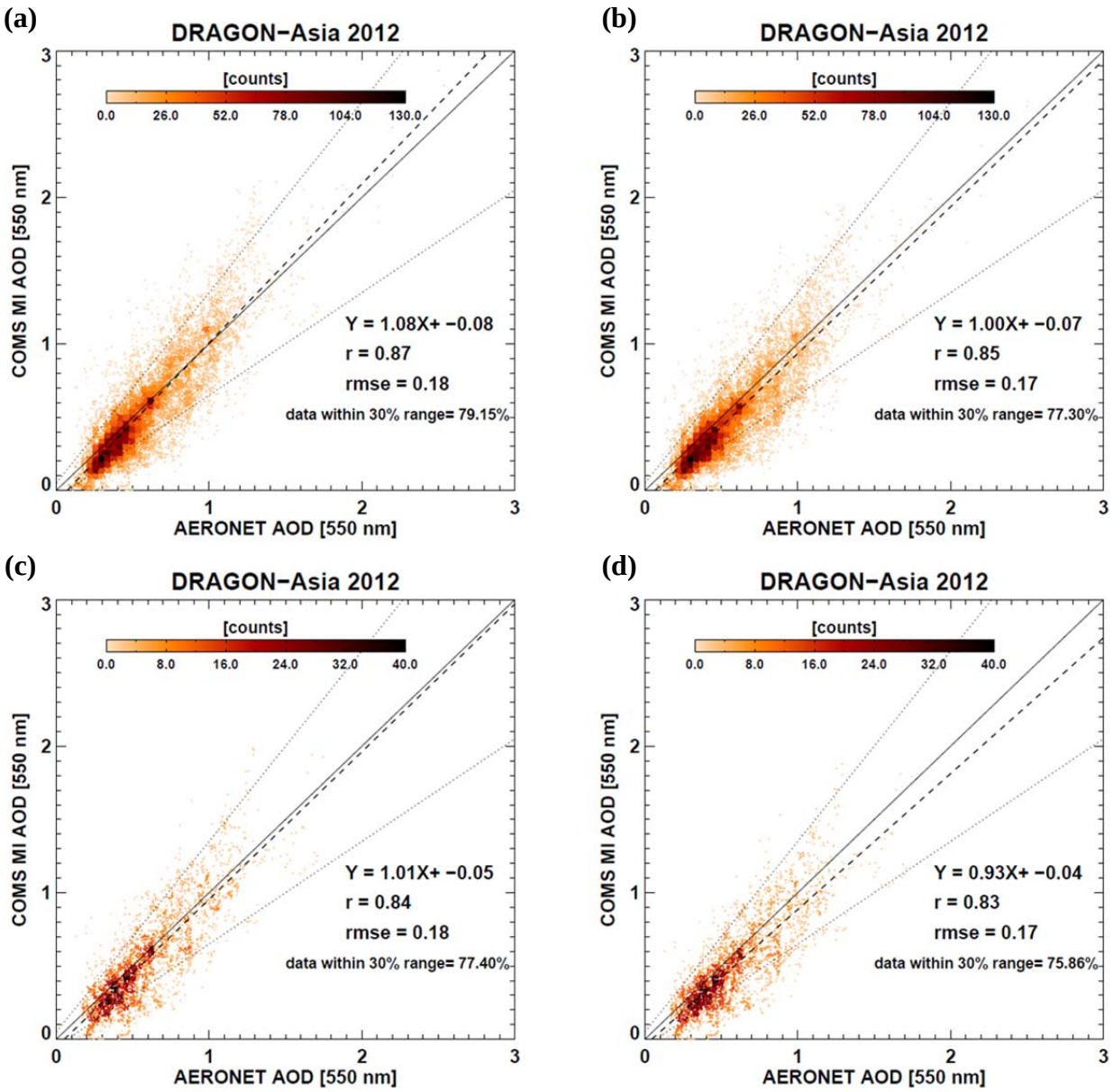

Figure 9. Evaluation of the AOD retrieved from MI measurements during DRAGON-Asia. The x-axis and y-axis indicate the values of AOD at 550 nm obtained from AERONET and MI measurements, respectively, and the color of the symbols shows the data counts for each AOD bin. The y-axis on the left [(a) and (c)] and right side [(b) and (d)] represents the AOD retrieved using the original and new LUT, respectively. The plots on the top [(a) and (b)] contain the data measured from all campaign sites, whereas those on the bottom [(c) and (d)] contain only the values from the sites excluded in the AOP analysis. The linear regression line with a Pearson coefficient (r) and root mean square error (RMSE) were included for each plot.

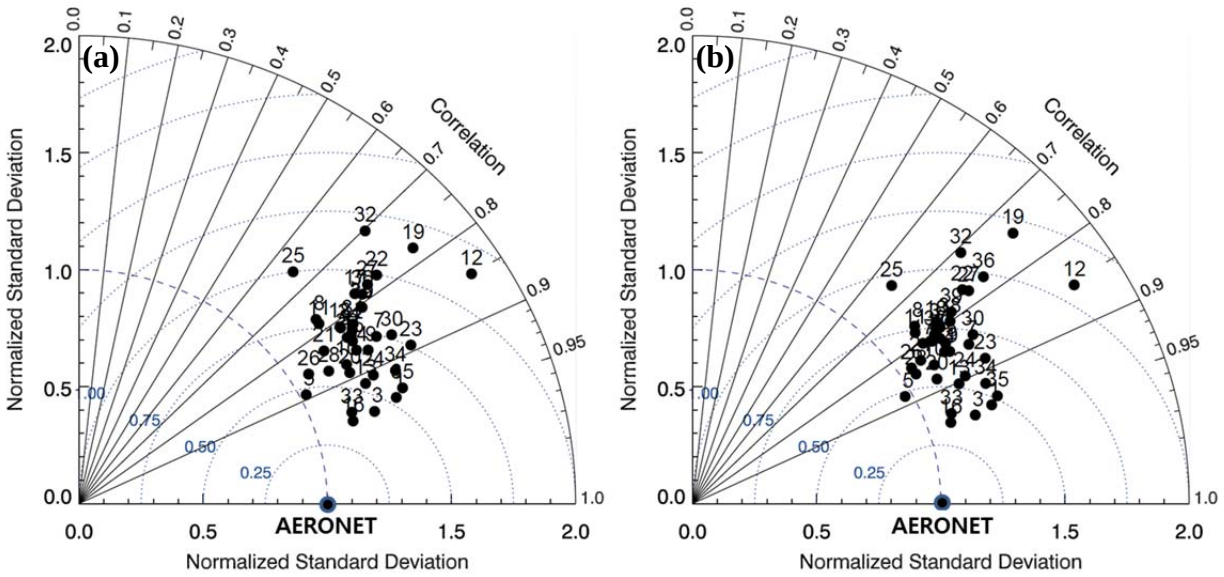

Figure 10. Taylor diagrams comparing the retrieved AODs and the values obtained from AERONET sun-photometer measurements during the DRAGON-2012 campaign. (a): Comparison of results from the original AOD, (b): comparison of results from the new AOD. The numbers above each symbol indicate the number of the DRAGON-Asia site, as listed in Table 1.

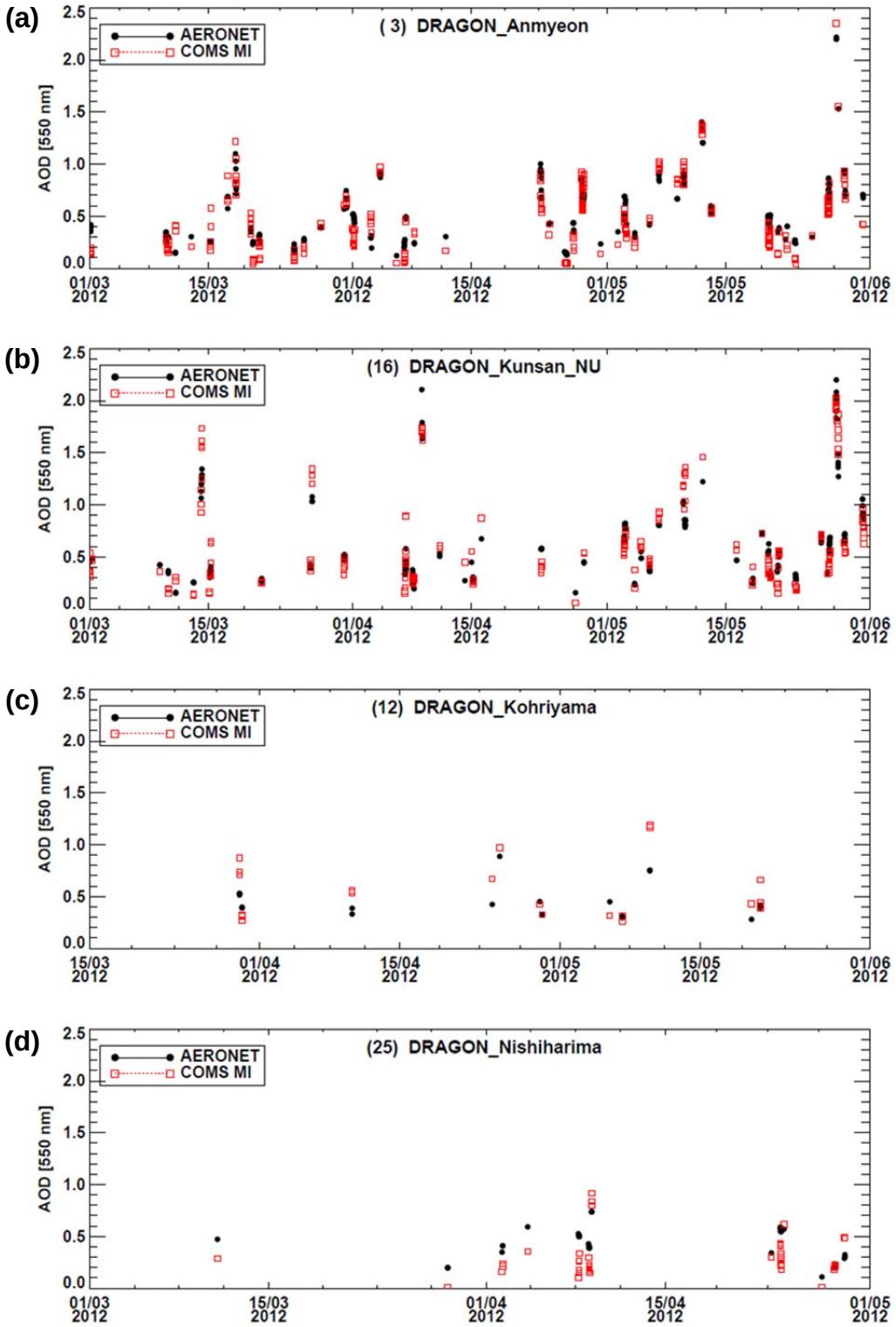

Figure 11. Temporal variations of AODs during the DRAGON-Asia. The red box and black circle represent the values retrieved from MI and AERONET measurement, respectively, and each panel shows the time series for different AERONET sites; (a) Anmyeon, (b) Kunsan_NU, (c) Kohriyama, (d) Nishiharima.